THE ASTROPHYSICAL JOURNAL, 433:96–116, 1994 September 20

DENSE CORES IN DARK CLOUDS. IX. OBSERVATIONS OF ^{13}CO AND C^{18}O IN VELA, CHAMAELEON, MUSCA, AND THE COALSACK

J. W. S. VILAS-BOAS[1]
Harvard-Smithsonian Center for Astrophysics and Centro de Aplicações Espaciais (CRAAE-INPE)
P. C. MYERS[1]
Harvard-Smithsonian Center for Astrophysics
AND
G. A. FULLER[2]
National Radio Astronomy Observatory
Received 1993 October 20; accepted 1994 March 28

ABSTRACT

One hundred one condensations with average optical size less than 7′ and visual extinction greater than 2.5 mag have been selected from ESO *J* plates, extinction maps, and catalogs of southern hemisphere dark clouds for observation in the ^{13}CO and C^{18}O $J = 1$–0 transitions. These regions are condensations in the dark molecular clouds Musca, Coalsack, Chamaeleon II, Chamaeleon III, and cometary globules in Vela and Gum nebula.

A search for *IRAS* point sources having colors of young stellar objects shows that these condensations have at most seven associated young stellar objects—far fewer than in Taurus and Ophiuchus. These 101 condensations generally have lower ^{13}CO and C^{18}O line intensity, C^{18}O optical depth, and ^{13}CO line width than do 90 condensations in Taurus, Ophiuchus, and Cepheus. Similarly, 47 of these southern condensations having star-count estimates of visual extinction generally have less extinction than do the 19 condensations in Taurus having extinction estimated by the same method.

The C^{18}O to ^{13}CO line-width ratio for the cometary globules in the Vela region is greater than for the other clouds, indicating that the ^{13}CO line width observed toward dark cloud condensations is related to the more extended and less dense intercondensation gas. Radial velocities suggest that the system of Vela globules has velocity dispersion 4.7 km s^{-1}, which is at least 2 times greater than the dispersion determined from formaldehyde observations. The Musca filament has velocities which are slightly higher—by $\sim$0.5 km s^{-1}—in the center than at the ends of the filament. Chamaeleon III has a 0.2 km s^{-1} pc^{-1} velocity gradient, and Chamaeleon II has no indication of velocity gradients. The Chamaeleon clouds and the Musca filament appear close to virial equilibrium.

Subject headings: ISM: clouds — ISM: kinematics and dynamics — ISM: molecules

1. INTRODUCTION

After their detection in interstellar clouds, the millimeter wavelength rotational lines of carbon monoxide and of its isotopic varieties have been widely used to probe dense condensations in nearby dark clouds, especially using the optically thin transitions of ^{13}CO and C^{18}O. The first and most extended CO survey of dense condensations in these lines was conducted by Myers, Linke, & Benson (1983, hereafter MLB) in the direction of 90 northern hemisphere positions especially in Taurus and Ophiuchus. The clouds surveyed by MLB were chosen by visual inspection of the Palomar Sky Prints, and were identified primarily as complexes of obscuration.

A survey of ^{13}CO and C^{18}O in 51 cloud condensations was also carried out by Nozawa et al. (1991) in the north of Ophiuchus by using results of a ^{12}CO unbiased survey as a guide.

A survey of 33 high-latitude cirrus clouds in ^{13}CO and C^{18}O (Turner, Xu, & Rickard 1992) showed dense condensations with properties comparable to those in dark clouds with some of them probably unstable to gravitational collapse.

Thus a total of 174 condensations have been studied in northern hemisphere dark clouds and high-latitude cirrus clouds, using molecular lines tracing gas with density $1–3 \times 10^3$ cm^{-3}. Almost all condensations observed are regions of high extinction.

These observations gave important information about the physics of dense condensations and their relation to the properties of stars forming inside them (Myers & Fuller 1992). Also, models of low-mass star formation based on the properties of such condensations have been successful in predicting the infrared spectra of embedded stars (Shu, Adams, & Lizano 1987).

Still, many aspects of the star formation process remain unclear. Molecular cloud complexes as well as different parts of an extended molecular dark cloud differ widely in their star-forming activity. More detailed studies of condensations, within a complex and from complex to complex, are needed to define relations among clouds, condensations, and stars.

Southern dark clouds have at least as much variety in star formation activity and structural complexity as do northern clouds. The relative numbers of *IRAS* sources, Herbig-Haro objects, and visible stars suggest that the Chamaeleon I, II, and III dark clouds are ranked in decreasing order of star formation activity, and perhaps evolution. No visible or embedded source have yet been identified in Chamaeleon III (Hetem,

[1] Harvard-Smithsonian Center for Astrophysics, Mail Stop 42, 60 Garden Street, Cambridge, MA 02138.
[2] NRAO, 949 North Cherry Avenue, Campus Building 65, Tucson, AZ 85721.

Sanzovo, & Lepine 1988; Schwartz 1977) and apparently there are no embedded stars in the Coalsack (Nyman, Bronfman, & Thaddeus 1991). Lupus has a relatively high proportion of low-mass M stars (Krautter 1991), while in Corona Australis there is a region with a high proportion of massive B stars (Taylor & Storey 1984). In Vela, several cometary globules are surrounded by a hot and ionized medium (Reipurth 1983; Zealey et al. 1983). These southern clouds differ greatly in their mass and structure, and their condensations form a good sample to be searched in order to understand the condensation physics, cloud dynamics, and variations from cloud to cloud. Yet very few condensations in southern dark clouds have been observed.

In this paper we present the first results of an extended survey of the ^{13}CO and $C^{18}O$ $J = 1$–0 rotational transitions conducted in optically selected condensations of the Vela region, Musca, Coalsack, and Chamaeleon II and III dark clouds. The main purpose of this survey is to compare condensation properties observed in these clouds with each other, and with those observed in Taurus, Ophiuchus, and Cepheus.

The selected positions are apparent maxima of visual extinction, with at least one dimension less than 7′. The source selection is described in § 2. In § 3 the CO observations are discussed, and in § 4 the methods of data reduction and analysis are presented. In §§ 5 and 6 are presented the observed and derived parameters of the sources which are compared with the same parameters for dense condensations observed in dark clouds by MLB. In § 7 are presented the results of a search for *IRAS* sources and pre–main-sequence stars associated with condensation positions observed in this survey. In § 8, general properties of the observed clouds, including stability and evolutionary aspects, are briefly discussed. The paper is summarized in § 9.

The main results are (1) the condensations observed in this survey have lower visual extinction and column densities than those observed in Taurus, Ophiuchus, and Cepheus. They also have weaker ^{13}CO and $C^{18}O$ emission and fewer *IRAS* sources associated. (2) The $C^{18}O$ to ^{13}CO line width ratio in Vela dense fragments (cometary globules), where the "intercondensation" gas density appear relatively low, is closer to one than in the other dark clouds. (3) Vela fragments seem to be distributed in a shell which is expanding with velocity up to 11 km s^{-1}, while Musca can be represented by a cylindrical filament with velocity gradient changing between 0.1 and -0.1 km s^{-1} pc^{-1} along its longer size. (4) The Chamaeleon clouds seem to be close to virial equilibrium, there is a velocity gradient of 0.2 km s^{-1} in Chamaeleon III, and no indication of velocity gradient in Chamaeleon II.

In this paper we will use the word "condensation," instead of "core," to denominate the selected regions because in the astronomical literature, cores are often considered to be regions with densities greater than 10^4 cm^{-3} (Myers 1985; Cernicharo 1991). In this survey only four positions satisfy this criterion. The word "fragment" is also avoided because it might imply the disruption of a more extended cloud.

2. SOURCE SELECTION

The positions observed in this survey are regions of visual extinction higher than 2 mag located in complexes of obscuration. A first list of sources was chosen with guidance of the star counts performed on ESO (B) plates by Hetem et al. (1988), using a grid of square elements with spatial resolution of 2′.25.

Using the Hetem et al. (1988) extinction maps, we identified the regions defined by the contour of visual extinction 2, 3, 4, or 5 mag located in the direction of Musca, Chamaeleon II, Coalsack, and Chamaeleon III with the smaller size less than or equal to 7′. Hereafter we refer to such regions as "condensations." Few condensations have been selected which have sizes bigger than 7′: five in Chamaeleon II with visual extinction 5.5, 5.1, 4.5, 4.0, and 3.8 and one in Musca with extinction 4.1. These are the most extended condensations with high visual extinction identified in these clouds, and they are almost round with average axial ratio 0.9. No condensations like these have been identified in Chamaeleon III and Coalsack. More than 70% of the condensations selected in these clouds have both dimensions less than or equal to 7′. Even in Vela, where the optical sizes of the condensations can be 65′, the densest parts of the cometary globules are smaller than 7′. When only one position with a higher extinction than the contour level was found in one of these regions, this extinction was attributed to the condensation, the coordinates of the region were chosen to be coincident with the high extinction position independently of its geometry, and the size of the condensation was assumed to be defined by the lower extinction contour. For condensations with circular or square shapes and with relatively uniform visual extinction, the position was defined as the geometrical center of the extinction distribution.

To find the coordinates of the condensations, we identified the position of four reference stars in each extinction map. As the plane projection of the equatorial coordinates for the clouds close to the Celestial pole are curved lines, the coordinates of the reference stars were converted to Galactic coordinates and an overlay was drawn, from which the coordinates of the condensations have been determined. The uncertainty in the coordinates associated with using the overlay is less than 1′. The optical size of the condensations were defined by eye-fitting an ellipse to the extinction distribution.

A catalog of southern dark clouds, compiled from visual inspection of ESO/SERC Southern *J* plates (Hartley et al. 1986), was also used to select some dense condensations since the Hetem et al. (1988) star counts did not cover all southern clouds. Several condensations have been identified and their positions, with 10″ accuracy, were compared with the positions of the condensations identified from the extinction map of Hetem et al. (1988). Some difference is expected in these positions since the coordinates given by this catalog is the approximate centroid of the condensations which are defined as class A, B, and C. These classes correspond approximately to the Lynds opacity 6, 4 to 5, and 3 or less, respectively (Lynds 1962; see Table 1). In regions where we did not have star counts we used this catalog which gives also the optical size for each condensation. We selected 27 dark clouds in the Vela region classified as cometary globules, several positions in the Coalsack and one position in Musca and Chamaeleon II.

In Chamaeleon II, III, and Musca we also made visual inspection of the ESO *J* plates for high opacity regions. In a few cases the opaque regions are extended over tens of arcminutes and have distinct local minima in their diffuse brightness. In these cases the local minima were selected and their coordinates were determined using the positions of reference stars identified in the plates. The same procedure used to find the coordinates in the star count maps have been used here. The uncertainty in the coordinates associated with using the overlay is estimated to be less than 1′. These positions have been compared with those obtained from star counts. When

the difference in these coordinates was less than 2'.5, the position of the dark cloud was assumed to be the same as determined by visual inspection of the ESO plates. A total of four positions in Musca and nine positions in Chamaeleon II have been identified in the ESO J plates, and selected for observations, which are not coincident with the highest extinction positions in the star count maps. In these cases the sizes of the condensations were defined by the contour of highest visual extinction, which was also eye fitted by an ellipse.

We analyzed 10 condensations, identified in the Hartley et al. (1986) catalog and by Hetem et al. (1988), which had the same coordinates, in order to compare the condensation sizes obtained using the different procedures. The condensation size was defined as $(l \times b)^{0.5}$ where l and b are the smaller and larger optical size. We concluded that the condensation dimensions are almost the same when their estimated sizes are less than or equal to 12'. In this interval are almost all condensations observed in this survey, except V6, V22, Cha 8, and Cha 18 for which the sizes are 12'.4, 19'.7, 12', and 14'.7, respectively. In this case, the condensations sizes defined using star counts can be 3 times smaller than the size estimated by Hartley et al. (1986). Some difference in size should also be expected due to the different definition of extinction used by Hartley et al. (1986) and Hetem et al. (1988).

3. CO OBSERVATIONS

The $J = 1$–0 ^{13}CO and C^{18}O observations were made in 1991 December 20–21 at the 15 m Swedish-ESO submillimeter telescope (SEST) at La Silla, Chile. The receiver front-end was based on a Schottky diode waveguide mixer followed by an intermediate-frequency amplifier. The SSB system temperature was typically 400 K. The acousto-optical spectrometer had a resolution of 43 KHz and a total bandwidth of 100 MHz. The spectra were taken by using overlap frequency switching mode (with 7 MHz frequency shift) and integrated for periods of 2 minutes in ^{13}CO and 10 minutes in C^{18}O. The observations were chopper-calibrated against a cold load to obtain the correction for atmospheric attenuation. Two independent receivers were used to obtain independent spectra which were recorded after every minute of integration time. The typical rms variations in antenna temperature corrected for atmospheric attenuation was 0.1 K for ^{13}CO and 0.06 K for C^{18}O, obtained by fitting the base line. The typical signal-to-noise ratio was higher than 10, the half-power beam width was 48″, and the adopted beam efficiency 0.9 as determined by van Dishoeck et al. (1991) and Gredel et al. (1994) observing the Moon. Intensity calibration was done against a load. The rms pointing accuracy, better than 10″, was checked systematically by observing SiO maser emission from VY CMa, IK Tau, and R Car.

The L1450 dark cloud was observed in ^{13}CO and C^{18}O and the results compared with the previous observations done by MLB. The average of the spectra obtained in one integration time showed a systematic difference of 0.4 km s^{-1} in radial velocity when compared to the MLB data. A detailed analysis of the spectra observed in this survey also shows a systematic difference of 0.2 km s^{-1} in radial velocity when the spectra obtained with both receivers used for these observations, are compared. This difference, probably due to nonlinearity of the photo-diode array, is negligible when averaging spectra with line width $\sim$1.5 km s^{-1}. However, if the observed line width is 0.40 km s^{-1}, the average of both spectra can overestimate this parameter by more than 40%. As the typical C^{18}O line width observed in this survey is 0.4–0.7 km s^{-1}, we did not average the spectra obtained with both receivers. The results presented in this work were obtained with the channel (A) showing the more linear signal-to-noise relation in the interval of observed antenna temperatures.

4. DATA REDUCTION AND ANALYSIS

The spectra were reduced using the Continuum and Line Analysis Single-Dish Software (Forveille, Guilloteau, & Lucas 1989). Each observed spectral line was fitted by a Gaussian function. The spectra with pronounced asymmetry or with peaks shifted by more than 0.7 km s^{-1} have been fitted with two Gaussian functions. In order to distinguish splitting due to saturation effects from splitting due to different ^{13}CO sources, lines split by less than 0.7 km s^{-1} were considered double only if the C^{18}O line is also double. In only one position (Cha 6) ^{13}CO showed a "rectangular" line shape; in that case the peak velocity, intensity, and full width at half-maximum were measured directly from the spectra.

To estimate the parameters of the spectral lines, the fitted base line was subtracted from the observed spectra. These lines were then analyzed to make estimates of the optical depth at the peak of the line, excitation temperature, and column density of C^{18}O in the cloud. The method used is the same used by MLB. Four basic assumptions are used to obtain the equations to derive the parameters of the spectral lines: (1) the product of beam efficiency times filling factor is the same for both ^{13}CO and C^{18}O, (2) the ^{13}CO and C^{18}O lines are formed in similar excitation conditions and the difference in the true value of the excitation temperatures T_{13} and T_{18} is less than the uncertainty in the deduced values due to the noise in the spectra, (3) in the observed positions the ^{13}CO to C^{18}O column density ratio is $\sim$5.5, which is the ratio of terrestrial abundances, and finally (4) in each cloud the observed ^{13}CO and C^{18}O lines are formed in regions with the same velocity gradient. Detailed discussion about these hypotheses are presented by MLB.

Using the definition of absorption coefficient in LTE conditions, the following equation relating the optical depth is obtained:

$$\frac{\tau_{13}}{\tau_{18}} = \frac{n_{13}(J=1) L_{13} \Delta V_{18} J(T_{18})}{n_{18}(J=1) L_{18} \Delta V_{13} J(T_{13})}, \quad (1)$$

where τ is the optical depth at the center of the line, ΔV is the line full width at half-maximum, L is the line-of-the sight extent of the source, and $J(T) = T_0/[\exp(T_0/T) - 1]$, where $T_0 = h\nu/k$, ν is the transition frequency and h and κ are the constants of Planck and Boltzmann, respectively. The subscripts specify the isotopic variety. Using this equation and the four assumptions above, we find $\tau_{13} = 5.5\tau_{18}$. Using assumption 1, the intensity ratio of both transitions obtained from the one-dimensional equation of radiative transfer in a homogeneous medium, is

$$\frac{T^*_{a13}}{T^*_{a18}} = \frac{[1 - \exp(-5.5\tau_{18})]}{[1 - \exp(-\tau_{18})]}, \quad (2)$$

where Ta^* is the observed antenna temperature corrected for atmospheric opacity. This ratio is identically equal to the corresponding ratio of main-beam brightness temperatures. From this equation we calculate τ_{18} using the ratio of observed antenna temperature. The excitation temperature is obtained from the solution of the radiative transfer equation and was

calculated by the equation:

$$\frac{T_0}{T_{18}} = \ln\left\{1 + \frac{T_0}{J(T_{bg}) + T^*_{a18}/[\eta_b \Phi(1 - e^{-\tau_{18}})]}\right\}, \quad (3)$$

where $T_{bg} = 2.7$ K (background radiation), η_b, which is 0.9 (van Dishoeck et al. 1991; Gredel et al. 1994) for the SEST telescope, and Φ is the filling factor which is assumed to be 1, since the emitting regions are bigger than the half-power beam width (48″).

From the definition of optical depth, assuming constant absorption throughout the cloud and that the observed lines have Gaussian shape the $C^{18}O$ column density in the $J = 1$ level can be written as

$$N_{18}(J = 1) = 3.6 \times 10^{14} \tau_{18} J(T_{18}) \Delta v_{18} \text{ cm}^{-2}. \quad (4)$$

where Δv is in km s^{-1}. This equation was used to estimate the column density of the observed lines. Although some ^{13}CO line asymmetry are observed in several sources, the $C^{18}O$ spectral lines are almost symmetrical and consequently there is negligible uncertainty in the column density due to the line shape. Observe that this parameter is calculated for only one rotational state. In order to estimate the total column density, the fraction of molecules in different rotational levels, which is a function of the excitation temperature, should be calculated, summed, and multiplied by $N_{18}(J = 1)$, as described by MLB.

5. OBSERVATIONAL RESULTS

The clouds observed in this survey, except Coalsack which is in the Galactic plane, have absolute Galactic latitude $> 6.^{\circ}7$. The observational results obtained in the direction of 101 condensations identified in Vela, Musca, Coalsack, and Chamaeleon II and III are shown in Table 1. In column (1) are given the names of the dark clouds; in columns (2) and (3), a number and the name given to each condensation; in columns (4) and (5) the equatorial coordinate; in columns (6), (7), and (8) are given the antenna temperature, radial velocity, and line width for the ^{13}CO line. In columns (9), (10), and (11) are given the same parameters for the $C^{18}O$; and in columns (12), (13), and (14) are given the optical depth, the excitation temperature, and the column density obtained from the $C^{18}O$ line. Column (15) gives some notes about the observed line profile. The estimated uncertainty in antenna temperature, radial velocities, and line width at half-maximum are given in brackets and correspond to the last digit of the fitted parameters. They were calculated following the method presented by Landman, Roussel-Dupre, & Tanigawa (1982).

The following discussion compares results reported here with those in northern dark clouds (MLB). The two groups form a useful comparison because the MLB sample of northern clouds have greater star formation activity than does the present sample of southern clouds. In order to compare the data of both surveys the observed antenna temperatures should be divided by the main beam efficiency which is 0.9 for these observations and 0.8 for MLB. The difference in efficiency is responsible for a difference of less than 13% in the observed antenna temperature.

5.1. *Antenna Temperatures*

In Figure 1 are plotted the distributions of ^{13}CO and $C^{18}O$ antenna temperatures and the ratio of these temperatures observed by MLB, and this survey. The peak of the ^{13}CO and $C^{18}O$ antenna temperature distributions are 2.5 and 0.45 K, respectively. For this survey the ^{13}CO and $C^{18}O$ antenna temperatures are in the intervals between 1–6 and 0.1–2 K, respectively, while the same parameters observed by MLB were detected in an interval 2–3 times wider. The typical line in this survey is weaker than in the MLB survey by 2 K for ^{13}CO and 1.2 K for $C^{18}O$. The positions observed in this survey shows a lower antenna temperature dispersion around the peak positions than do the MLB data. Although the distribution of antenna temperatures in this survey is more concentrated around the distribution peaks the ratio of these parameters are distributed in a wide interval with more than 10 condensations peaking at antenna temperature ratios higher than 10.

5.2. *Line Width and Shape*

The histogram in Figure 2 shows that ^{13}CO and $C^{18}O$ line width distributions have peak values 0.8 and 0.5 km s^{-1}, respectively. The line widths were not corrected for instrumental resolution, because they are significantly greater than the resolution (0.12 km s^{-1}). The widths are more concentrated around the peak of the distribution than the same parameters observed by MLB. The peak position of these distributions is coincident for $C^{18}O$, for ^{13}CO it is 0.4 km s^{-1} shifted to lower line width. Vela has the smallest ^{13}CO line width (0.7 km s^{-1}) while its $C^{18}O$ line width (0.6 km s^{-1}) seems not to be different from the other clouds. Among the clouds in this survey, Chamaeleon has the widest average line width (1 and 0.7 km s^{-1} for ^{13}CO and $C^{18}O$, respectively).

The region with the lowest average ^{13}CO line width is Vela while the lowest value of this parameter for $C^{18}O$ was observed in Coalsack and Musca. The line widths observed in Chamaeleon II and Chamaeleon III are similar in ^{13}CO and $C^{18}O$.

Except V14, in all other positions observed in Vela the line profiles are symmetrical, and the ^{13}CO line width is lower than 0.9 km s^{-1}. In V3, V4, and V25 the line width is bigger in $C^{18}O$ than ^{13}CO, and they are equal in V5. Approximately equal line widths were also observed in Mu 6 and Cha 7, but in these positions the signal-to-noise ratios are poor. In V25 the line profile shows wings in high and low velocity sides of the spectra. In all spectra observed in Vela there is no evidence of line saturation effects, and the line-width dispersion (0.17 km s^{-1}) is the lowest in this survey.

The lines observed in Coalsack are also symmetric, except in Cos 5 where the ^{13}CO line shows weak asymmetry, and there is no indication of line wings. In Musca the spectra are also symmetric, except in Mu 3, where the line is weakly asymmetric to high velocities, and Mu 13 where the ^{13}CO and $C^{18}O$ lines are split, suggesting two distinct emission regions (Fig. 3). Weak evidence of saturation in the ^{13}CO line can be seen in Mu 1 and Mu 5, where the peaks of the lines are flat, departing from Gaussian shape. In Chamaeleon II and III the ^{13}CO line profiles are more complex, showing strong asymmetries, line wings, and split lines in several positions.

The narrowest $C^{18}O$ line width (0.34 km s^{-1}) was observed in V23 where 20 K is a lower limit to the $C^{18}O$ excitation temperature. The observed line width is then 3 times larger than the thermal width, assuming local thermodynamic equilibrium. In $\sim 50\%$ of the sources observed in ^{13}CO and $C^{18}O$, the excitation temperature is higher than 20 K, and there is no correlation between this parameter and the observed line width. In four positions where the line width is lower than 0.4 km s^{-1}, two have excitation temperatures higher than 20 K and two lower than 10 K.

The $C^{18}O$ and ^{13}CO line width generally increase together, although the increase in the $C^{18}O$ width with respect to the

1994ApJ...433...96V

TABLE 1

OBSERVED CONDENSATIONS IN THE SOUTHERN HEMISPHERE CLOUDS

Cloud	Source		RA (1950) (h, m, s)	DEC (1950) (deg, m, s)	13CO Ta* (K)	13CO Vlsr (km/s)	13CO FWHM (km/s)	C18O Ta* (K)	C18O Vlsr (km/s)	C18O FWHM (km/s)	Optical Depth	T18 (K)	N18 1.00E+15 (cm-2)	NOTE
VELA	1	V1	07 14 28	-43 52 18	4.52 [1]	4.33 [0.5]	0.66 [0.8]	0.77 [5]	4.23 [2]	0.48 [3]	0.03	> 20	0.23	
	2	V2	07 26 20	-50 58 18	3.57 [1]	-0.38 [0.8]	0.74 [1]	0.88 [3]	-0.43 [1]	0.55 [2]	0.15	10	0.57	
	3	V3	07 27 53	-41 04 12	3.86 [0.1]	-0.79 [0.5]	0.72 [0.7]	0.49 [7]	-0.92 [5]	0.85 [6]	0.01	> 20	0.13	
	4	V4	07 29 05	-46 37 18	3.49 [1]	1.16 [0.8]	0.78 [1]	0.43 [4]	1.15 [3]	0.97 [5]	0.01	> 20	0.15	
	5	V5	07 31 03	-50 39 06	2.34 [2]	-0.39 [1]	0.59 [2]	0.41 [8]	-0.43 [3]	0.50 [4]	0.03	19	0.22	
	6	V6	07 32 41	-46 47 42	4.29 [1]	1.82 [0.7]	0.74 [1]							
	7	V7	07 37 18	-49 43 48	2.74 [2]	-0.53 [1]	0.61 [1]	0.47 [4]	-0.57 [4]	0.56 [6]	0.03	21	0.28	
	8	V8	07 37 42	-47 46 12	3.86 [1]	0.34 [0.7]	0.75 [1]	0.66 [3]	0.32 [2]	0.64 [3]	0.03	> 20	0.30	
	9	V9	07 39 16	-43 42 06	1.59 [3]	-3.23 [1]	0.55 [2]	0.39 [8]	-3.21 [3]	0.46 [4]	0.15	6	0.23	
	10	V10	07 40 51	-41 58 00	1.02 [4]	-3.50 [3]	0.96 [4]	0.06 -	- -	- -				f
	11	V11	07 41 26	-42 00 18	3.01 [1]	-4.80 [0.9]	0.77 [1]	0.29 [7]	-4.80 [5]	0.79 [7]	0.01	> 20	0.12	
	12	V12	07 41 56	-42 14 48	2.96 [2]	-4.35 [1]	0.72 [1]	0.31 [12]	-4.36 [4]	0.45 [6]	0.01	> 20	0.07	
	13	V13	08 07 04	-35 50 30	3.24 [1]	6.19 [1]	0.96 [1]	0.33 [8]	6.24 [5]	0.72 [7]	0.01	> 20	0.11	
	14	V14	08 07 39	-35 55 54	4.34 [0.8]	6.31 [0.8]	1.19 [1]	0.99 [2]	6.29 [1]	0.90 [2]	0.12	13	1.03	
	15	V15	08 10 25	-33 47 12	1.14 [5]	5.76 [2]	0.56 [3]							
	16	V16	08 10 27	-33 51 60	2.96 [2]	5.64 [0.8]	0.58 [1]	0.50 [5]	5.57 [2]	0.47 [3]	0.03	> 20	0.22	
	17	V17	08 10 28	-33 36 36	2.88 [2]	5.38 [0.9]	0.55 [1]							
	18	V18	08 12 26	-34 21 42	3.72 [1]	5.06 [0.7]	0.77 [1]	0.88 [3]	5.01 [2]	0.66 [2]	0.12	12	0.68	
	19	V19	08 13 32	-33 55 30	1.39 [4]	1.99 [1]	0.45 [2]							
	20	V20	08 14 03	-33 41 30	2.88 [2]	2.38 [0.9]	0.65 [1]	0.74 [5]	2.26 [2]	0.48 [3]	0.18	8	0.44	
	21	V21	08 17 32	-42 45 18	1.75 [3]	-12.02 [2]	0.87 [3]							b
	22	V22	08 26 48	-33 35 48	4.63 [1]	6.87 [0.7]	0.74 [1]	0.76 [3]	6.89 [2]	0.63 [2]	0.03	> 20	0.30	
	23	V23	08 35 23	-36 27 24	3.00 [1]	10.75 [0.6]	0.68 [0.8]	0.49 [6]	10.75 [2]	0.34 [3]	0.03	> 20	0.16	b
	24	V24	08 51 04	-50 28 42	1.85 [3]	2.33 [1]	0.45 [2]							
	25	V25	08 51 04	-51 40 30	3.05 [2]	3.98 [0.8]	0.56 [1]	0.33 [7]	3.95 [4]	0.73 [6]	0.01	> 20	0.12	
	26	V26	09 12 13	-42 17 36	0.09 -	- -	- -							f
	27	V27	09 20 29	-45 36 00	2.42 [2]	-1.13 [1]	0.97 [2]	0.75 [3]	-1.17 [2]	0.68 [2]	0.27	7	0.78	
MUSCA	28	Mu1	12 18 52	-72 05 25	2.94 [1]	2.81 [1]	1.06 [2]	0.35 [7]	2.88 [3]	0.55 [5]	0.01	> 20	0.09	
	29	Mu2	12 18 53	-71 44 50	2.12 [3]	2.97 [1]	0.47 [2]	0.06						
	30	Mu3	12 19 28	-71 51 57	2.78 [2]	3.01 [1]	0.88 [2]	0.50 [6]	2.94 [2]	0.38 [3]	0.03	> 20	0.18	
	31	Mu4	12 21 29	-71 35 56	3.81 [1]	3.42 [0.8]	0.74 [1]	1.22 [2]	3.42 [0.9]	0.50 [1]	0.30	8	0.77	
	32	Mu5	12 22 30	-71 24 38	3.66 [1]	3.52 [1]	0.86 [1]	1.44 [2]	3.61 [0.7]	0.50 [1]	0.45	8	1.15	
	33	Mu6	12 23 20	-71 09 60	3.04 [2]	3.42 [0.8]	0.53 [1]	0.19 [10]	3.32 [7]	0.54 [10]	0.01	> 20	0.09	
	34	Mu7	12 25 32	-71 02 44	4.01 [1]	3.62 [0.8]	0.85 [1]	0.82 [3]	3.64 [1]	0.64 [2]	0.06	19	0.57	
	35	Mu8	12 26 19	-70 54 13	3.90 [1]	3.70 [0.7]	0.74 [1]	1.28 [2]	3.80 [0.7]	0.38 [1]	0.33	8	0.64	
	36	Mu9	12 27 50	-70 54 01	4.02 [1]	3.73 [[0.9	1.05 [1]	1.10 [2]	3.60 [1]	0.59 [1]	0.21	10	0.85	
	37	Mu10	12 27 57	-70 46 18	3.62 [1]	3.75 [0.9]	0.96 [1]	1.51 [2]	3.91 [0.7]	0.39 [1]	0.48	8	0.96	
	38	Mu11	12 28 42	-70 45 07	3.85 [1]	3.64 [0.7]	0.76 [1]	1.29 [2]	3.67 [0.8]	0.41 [1]	0.33	8	0.69	
	39	Mu12	12 29 31	-70 28 55	2.14 [2]	4.01 [2]	0.84 [2]							

TABLE 1—*Continued*

Mol. Coud		Source	RA (1950) (h, m, s)	DEC (1950) (deg, m, s)	13CO Ta* (K)	13CO Vlsr (km/s)	13CO FWHM (km/s)	C18O Ta* (K)	C18O Vlsr (km/s)	C18O FWHM (km/s)	Optical Depth	T18 (K)	N18 1.00E+15 (cm-2)	NOTE
	40	Mu13	12 32 05	-70 24 15	3.94 [1]	3.55 [0.8]	0.72 [1]	0.60 [5]	3.47 [2]	0.41 [2]	0.01	> 20	0.06	
					2.42 [2]	4.39 [1]	0.59 [2]	0.27 [10]	4.24 [5]	0.57 [6]	0.01	> 20	0.09	
	41	Mu14	12 33 01	-69 52 45	0.09 -	- -	- -							f
	42	Mu15	12 33 15	-70 17 03	3.07 [1]	3.36 [1]	1.18 [2]	0.31 [8]	3.19 [4]	0.57 [5]	0.01	> 20	0.09	c
	43	Mu16	12 34 24	-70 13 59	0.36 [20]	2.78 [8]	0.53 [12]							
COAL SACK	44	CoS1	12 19 21	-66 10 30	2.69 [2]	-5.42 [1]	0.56 [2]	0.53 [5]	-5.46 [2]	0.50 [3]	0.04	18	0.28	
	45	CoS2	12 28 28	-63 28 22	4.00 [1]	-5.46 [0.8]	0.86 [1]	1.15 [2]	-5.48 [1]	0.62 [2]	0.24	9	0.89	
	46	CoS3	12 30 12	-63 33 54	4.50 [1]	-5.66 [0.8]	0.73 [1]	1.07 [2]	-5.69 [0.9]	0.44 [1]	0.12	14	0.55	
	47	CoS4	12 30 57	-63 23 12	3.00 [2]	-5.34 [2]	1.24 [2]	1.01 [3]	-5.53 [1]	0.51 [1]	0.33	7	0.71	
	48	CoS5	12 40 12	-61 49 36	3.47 [2]	-3.93 [1]	0.74 [2]	0.33 [8]	-4.02 [4]	0.64 [6]	0.01	> 20	0.10	b
	49	CoS6	12 55 27	-66 08 24	2.56 [2]	-22.44 [2]	1.06 [3]							d,a
	50	CoS7	12 55 51	-61 04 06	2.57 [3]	-0.80 [2]	0.75 [2]	0.57 [4]	-0.82 [1]	0.44 [2]	0.09	11	0.31	
	51	CoS8	13 09 02	-64 09 48	0.50 [1]	-8.49 [9]	0.88 [10]							
	52	CoS9	13 09 07	-64 49 00	2.63 [2]	-26.12 [1]	1.04 [2]							d
	53	CoS10	13 15 31	-62 26 12	3.49 [1]	-29.62 [2]	2.05 [2]							d
	54	CoS11	13 16 05	-64 19 30	1.09 [5]	-23.52 [3]	0.71 [4]							
	55	CoS12	13 16 15	-62 17 42	4.92 [0.9]	-31.84 [1]	1.67 [2]							d
	56	CoS13	13 17 00	-64 57 18	1.95 [3]	-7.20 [2]	0.69 [3]							
	57	CoS14	13 21 31	-63 27 18	2.35 [2]	-20.95 [1]	0.82 [2]							d
CHAM. II	58	Cha1	12 44 15	-76 33 00	1.84 [2]	3.55 [3]	1.73 [4]							c
	59	Cha2	12 45 23	-76 30 50	1.96 [2]	3.64 [2]	1.32 [3]							a
	60	Cha3	12 45 25	-77 05 24	1.41 [3]	3.29 [4]	1.62 [5]							a
	61	Cha4	12 46 28	-76 35 60	2.31 [2]	3.55 [2]	1.28 [3]	0.62 [4]	3.55 [2]	0.44 [2]	0.18	7	0.34	
	62	Cha5	12 48 01	-76 37 01	2.69 [2]	3.34 [2]	1.61 [3]	1.24 [2]	3.21 [1]	0.61 [2]	0.57	6	1.18	c
	63	Cha6	12 48 12	-76 56 37	2.20 -	2.95 -	1.80 -							e
	64	Cha7	12 49 47	-76 54 39	1.52 [4]	2.51 [2]	0.50 [2]	0.40 [7]	2.72 [3]	0.59 [5]	0.18	6	0.36	
					2.88 [1]	3.19 [2]	1.58 [2]	0.56 [4]	3.42 [3]	1.07 [5]	0.03	> 20	0.51	
	65	Cha8	12 49 51	-76 47 24	2.91 [1]	3.04 [1]	1.18 [2]	0.70 [4]	0.32 [2]	0.59 [3]	0.12	10	0.49	
	66	Cha9	12 50 48	-76 18 35	0.90 [4]	2.51 [5]	1.59 [7]							a
	67	Cha10	12 51 08	-76 55 14	2.69 [2]	3.05 [2]	1.12 [2]	0.48 [6]	3.15 [3]	0.65 [4]	0.31	4	0.12	
					0.58 [6]	2.25 [8]	1.82 [12]	0.19 [16]	2.32 [7]	0.51 [10]	0.01	> 24	0.11	
	68	Cha11	12 51 12	-76 29 30	2.57 [1]	3.69 [1]	1.31 [2]							b
	69	Cha12	12 52 38	-76 34 30	2.04 [2]	3.39 [2]	0.89 [2]							
					0.61 [7]	1.69 [5]	0.81 [7]							
	70	Cha13	12 53 20	-77 12 00	2.08 [2]	2.83 [3]	1.82 [4]							a
	71	Cha14	12 53 30	-76 22 60	1.41 [3]	3.69 [3]	1.00 [4]							
	72	Cha15	12 54 02	-75 51 27	2.19 [3]	2.10 [2]	0.75 [2]							
	73	Cha16	12 55 16	-77 12 20	2.26 [2]	3.08 [3]	2.06 [4]	0.14 [13]	2.71 [14]	1.29 [20]	0.01	> 20	0.20	a

TABLE 1—*Continued*

Mol. Coud	Source	RA (1950) (h, m, s)	DEC (1950) (deg, m, s)	13CO Ta* (K)	13CO Vlsr (km/s)	13CO FWHM (km/s)	C18O Ta* (K)	C18O Vlsr (km/s)	C18O FWHM (km/s)	Optical Depth	T18 (K)	N18 1.00E+15 (cm-2)	NOTE
	74 Cha17	12 56 14	-77 00 00	3.09 [1]	3.92 [1]	1.12 [2]	1.14 [3]	4.01 [1]	0.53 [2]	0.39	7	0.88	
	75 Cha18	12 56 20	-76 55 26	3.46 [1]	3.59 [1]	1.13 [2]	1.23 [2]	3.69 [0.9]	0.53 [1]	0.36	8	0.97	
	76 Cha19	12 57 45	-77 01 10	3.35 [1]	3.75 [1]	1.08 [1]	1.20 [3]	3.74 [1]	0.59 [2]	0.39	7	0.98	
	77 Cha20	12 59 06	-77 06 20	3.16 [2]	3.85 [1]	0.69 [2]	1.08 [3]	3.86 [0.9]	0.53 [1]	0.33	7	0.74	
	78 Cha21	12 59 23	-77 23 50	1.22 [4]	3.38 [3]	1.04 [5]							c
	79 Cha22	12 59 53	-77 42 45	1.08 [5]	2.04 [3]	0.73 [4]							
				1.61 [3]	4.04 [2]	0.94 [3]							
	80 Cha23	13 00 26	-77 05 24	2.72 [2]	4.07 [1]	0.60 [1]							
	81 Cha24	13 01 21	-77 36 47	2.54 [2]	2.44 [1]	0.84 [2]	0.39 [7]	2.34 [3]	0.51 [4]	0.01	> 20	0.08	
				1.88 [2]	3.90 [2]	1.22 [3]							
	82 Cha25	13 02 00	-77 48 07	1.99 [3]	4.01 [2]	0.75 [2]							
				2.13 [3]	1.90 [1]	0.52 [2]							
	83 Cha26	13 03 18	-76 45 50	2.29 [2]	4.16 [2]	1.01 [2]							
	84 Cha27	13 03 20	-77 26 60	2.26 [2]	3.66 [2]	1.04 [2]							
	85 Cha28	13 03 46	-77 43 45	2.35 [2]	3.81 [2]	1.05 [2]							c
CHAM.III	86 Cha29	12 22 25	-79 06 60	3.01 [1]	1.91 [2]	1.30 [2]	0.95 [2]	1.89 [1]	0.95 [2]	0.30	7	1.21	c
	87 Cha30	12 23 27	-80 08 38	2.74 [2]	1.89 [2]	1.40 [3]	0.22 [8]	2.00 [7]	1.08 [10]	0.01	> 20	0.17	c
	88 Cha31	12 29 30	-80 17 60	2.27 [1]	1.93 [1]	1.20 [2]							a
	89 Cha32	12 32 00	-80 15 39	2.70 [2]	2.03 [2]	1.13 [2]	0.31 [9]	1.81 [5]	0.70 [7]	0.01	> 20		
				1.38 [5]	3.59 [2]	0.57 [3]							
	90 Cha33	12 37 50	-79 57 60	2.27 [2]	1.80 [2]	1.30 [3]	0.05 -	- -	- -				c,f
	91 Cha34	12 40 10	-79 43 00	2.25 [3]	1.47 [2]	0.72 [3]							a
	92 Cha35	12 40 40	-79 59 00	2.26 [2]	2.21 [2]	1.55 [3]	0.57 [4]	2.47 [2]	0.54 [3]	0.16	7	0.37	
	93 Cha36	12 41 15	-80 12 40	2.04 [2]	2.00 [2]	1.79 [3]	0.12 [11]	2.15 [24]	2.75 [35]	0.01	> 20	0.43	a
	94 Cha37	12 49 20	-79 42 00	3.47 [1]	1.61 [1]	1.24 [2]	0.90 [3]	1.62 [1]	0.53 [2]	0.18	6	0.32	b
	95 Cha38	12 49 37	-79 06 45	2.10 [2]	1.47 [2]	1.25 [3]							b
	96 Cha39	12 50 22	-79 17 60	2.21 [3]	1.30 [1]	0.65 [2]	0.12 [14]	1.20 [21]	1.90 [30]	0.01	> 20	0.30	
				2.65 [2]	2.15 [1]	0.72 [2]	0.29 [10]	2.20 [5]	0.58 [7]	0.01	> 20	0.09	
	97 Cha40	12 50 52	-79 11 15	2.32 [2]	1.30 [2]	1.33 [3]							
	98 Cha41	12 51 00	-79 29 00	2.87 [2]	2.09 [1]	1.01 [2]							
	99 Cha42	12 52 55	-78 40 00	1.55 [3]	1.56 [2]	0.93 [3]							
	100 Cha43	12 53 00	-78 51 27	1.88 [3]	1.61 [2]	0.80 [3]							
	101 Cha44	12 53 00	-79 01 07	2.10 [3]	1.05 [2]	0.95 [3]							

[a] Sources with asymmetric line profile.
[b] Sources with weakly asymmetric line profile.
[c] Sources with line peak split.
[d] Sources where the observed lines comes from sources behind the dark cloud.
[e] Sources with rectangular line profile.
[f] Sources in which only upper limits in intensity have been detected in one of the lines.

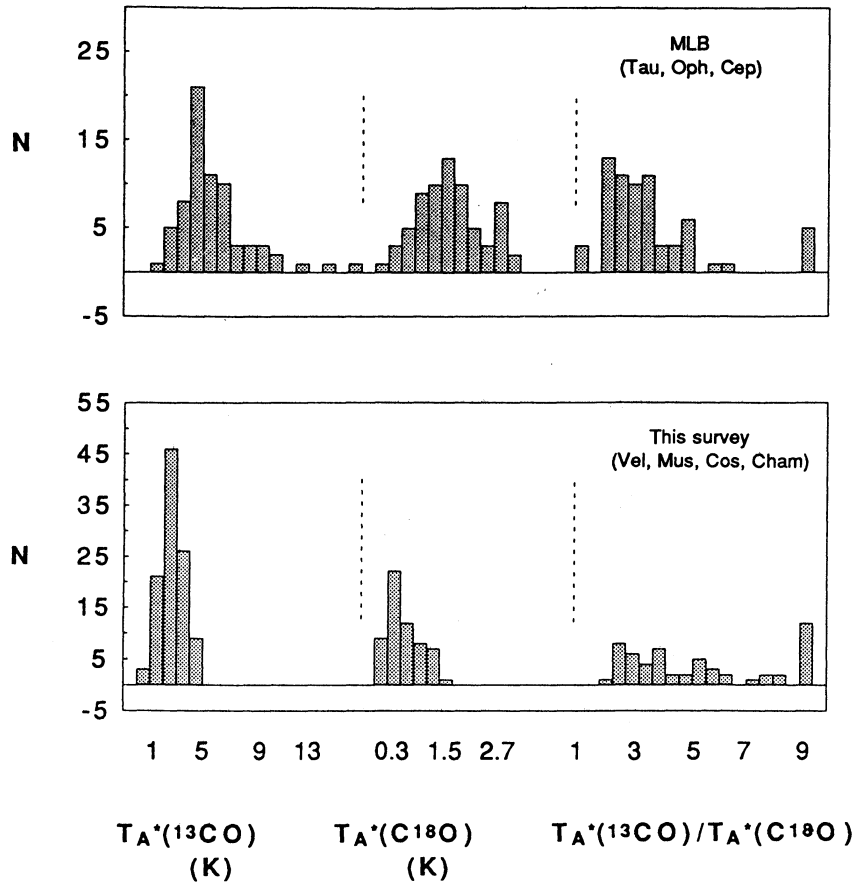

FIG. 1

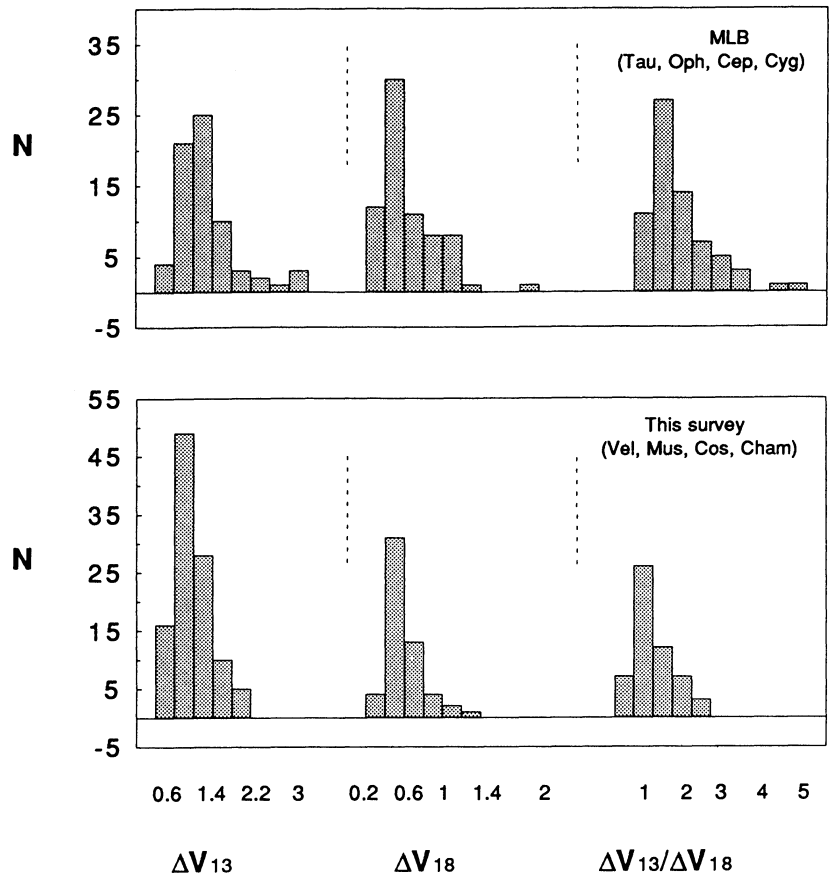

FIG. 2

FIG. 1.—Histograms of peak line antenna temperature corrected for atmospheric attenuation observed by MLB and this survey. The ^{13}CO and $C^{18}O$ antenna temperature distributions observed in this survey are shifted, with respect to MLB data, to lower values by 2 K and 1.2 K, respectively. The antenna temperature ratios have fewer low values in this survey than in the MLB survey. The dotted lines separate the different distributions.

FIG. 2.—Histograms of the distribution of line widths and line width ratios observed by MLB and this survey. The ^{13}CO line width observed in this survey is shifted, with respect to MLB data, to lower values by 0.4 km s^{-1}, while the $C^{18}O$ has same line width. The dotted lines separate the different distributions.

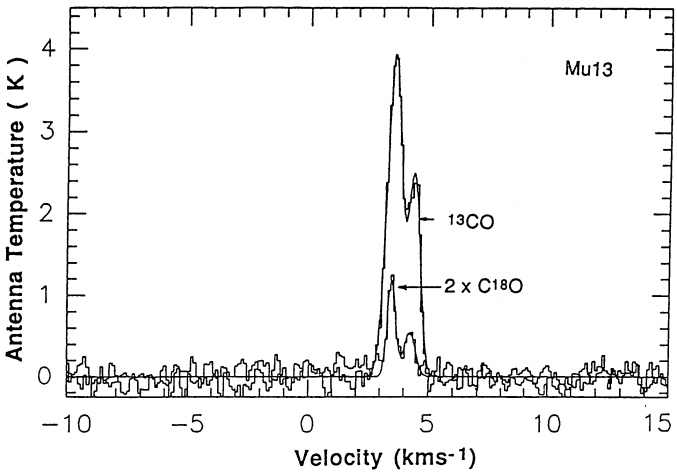

FIG. 3.—Spectra of ^{13}CO and $C^{18}O$ observed in Mu 13, which is the unique position in Musca where the spectra lines are split. The $C^{18}O$ spectrum is multiplied by a factor of 2 in order to be compared with ^{13}CO. Both spectra are fitted by Gaussian lines.

^{13}CO width is significantly greater in Vela than in Chamaeleon, Coalsack, and Musca. This last property is shown in Figure 4.

5.3. *Optical Depth*

The distribution of $C^{18}O$ optical depth (Fig. 5) is between 0 and 0.6. The peak is located in the 0–0.2 interval, and almost 70% of the sources have opacities lower than 0.2. The maximum value observed was 0.57 in Cham II, where the average optical depth is 0.22, with standard deviation 0.18, and with standard error of the mean 0.05. This is the highest averaged optical depth among the clouds observed in this survey. The smallest one, with average 0.07 and standard deviation 0.07, was observed in Vela where in several positions the optical depth is lower than 0.01. The distribution of optical depth is very concentrated around the peak position, indicating that the $C^{18}O$ emission observed in all positions in this survey is optically thin. Due to this low optical depth, the $C^{18}O$ lines width were not corrected for opacity broadening: for the highest opacity observed in this survey, in Cham II, the line-width correction for a Gaussian line shape is lower than 13%. Only in two positions in Musca was the opacity greater than 0.4. In all other positions the opacity was smaller, with average value lower than 0.1 and standard deviation 0.1.

In contrast, the $C^{18}O$ optical depths observed by MLB are higher: they span the interval between 0 and 1.6, with a few positions peaking between 1.2 and 1.6.

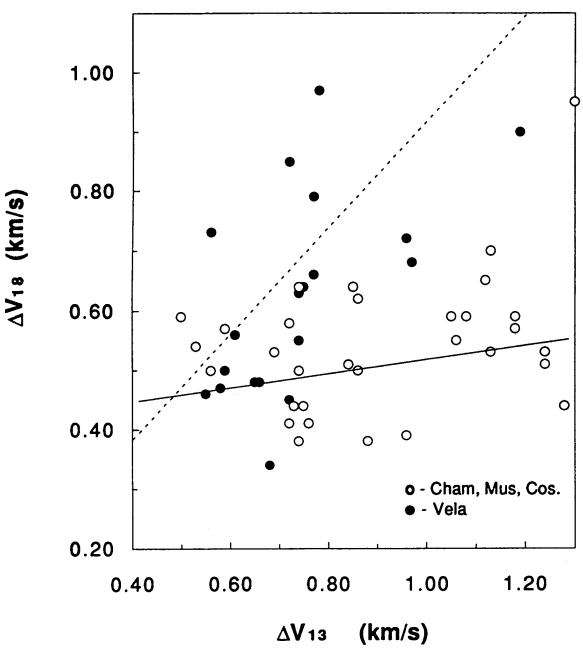

FIG. 4.—The $C^{18}O$ vs. ^{13}CO line widths observed in several condensations in this survey. The filled circles are positions observed in Vela, while open circles are positions observed in the other clouds. The dotted and solid lines are best fits for the Vela positions and the other dark clouds, respectively.

5.4. *Column Density*

The $C^{18}O$ column densities are lower than 10^{15} cm^{-2}, except in four positions, one in Vela, one in Musca, one in Cham II, and one in Cham III. The lowest estimated column density was 6×10^{13} cm^{-2} in Musca and the highest one was 1.2×10^{15} cm^{-2} in Cham III. The estimated column densities are uniformly distributed in the interval between 10^{14} cm^{-2} and 1.6×10^{15} cm^{-2}. In Figure 5 are plotted all $C^{18}O$ column densities, including those positions, where the optical depth was estimated as an upper limit. From the 60 positions observed in ^{13}CO and $C^{18}O$ only 32 had $C^{18}O$ column densities well determined; the rest have upper limits. The $C^{18}O$ column densities observed by MLB are larger, with mean 1.6×10^{15} cm^{-2}. The difference is due mainly to the difference in optical depth discussed above in § 5.3, and further in § 6.2.

5.5. *Excitation Temperature*

From a total of 101 condensations observed in ^{13}CO, 60 were observed in $C^{18}O$ and for 32 the excitation temperature was deduced. For the rest this temperature is a lower limit. The distribution of $C^{18}O$ excitation temperature (Fig. 5) shows a well-defined peak between 7 and 9 K. For 28 positions where the optical depth is an upper limit the excitation temperature is higher than 20 K. The lowest average excitation temperature (11 K) was found in Cham II, which is the cloud where the position with the lowest excitation temperature (4 K) was observed. The highest average excitation temperature (16 K) value was found in Vela.

6. DERIVED PARAMETERS OF THE SOURCES

The derived properties of the condensations observed in this survey are presented on Table 2. In columns (1) and (2) are given a number and the name of the condensations; in columns (3) and (4) the equatorial coordinates; in columns (5) and (6) are given optical estimates of the visual extinction corresponding to the observed positions (Hartley et al. 1986; Hetem et al. 1988) and their optical sizes in arcminutes. In columns (7) and (8) are given the distances and size of the source in parsecs; in column (9) are given the visual extinction estimated using the $C^{18}O$ column density; in columns (10) and (11) are given the column and volumetric densities of molecular hydrogen. Finally, in column (12), are given the masses estimated for the condensations. The procedure to calculate these parameters is discussed below.

6.1. *Column Density of Molecular Hydrogen*

To estimate the molecular hydrogen column density we used the well-known gas-to-dust relation of Bohlin, Savage, &

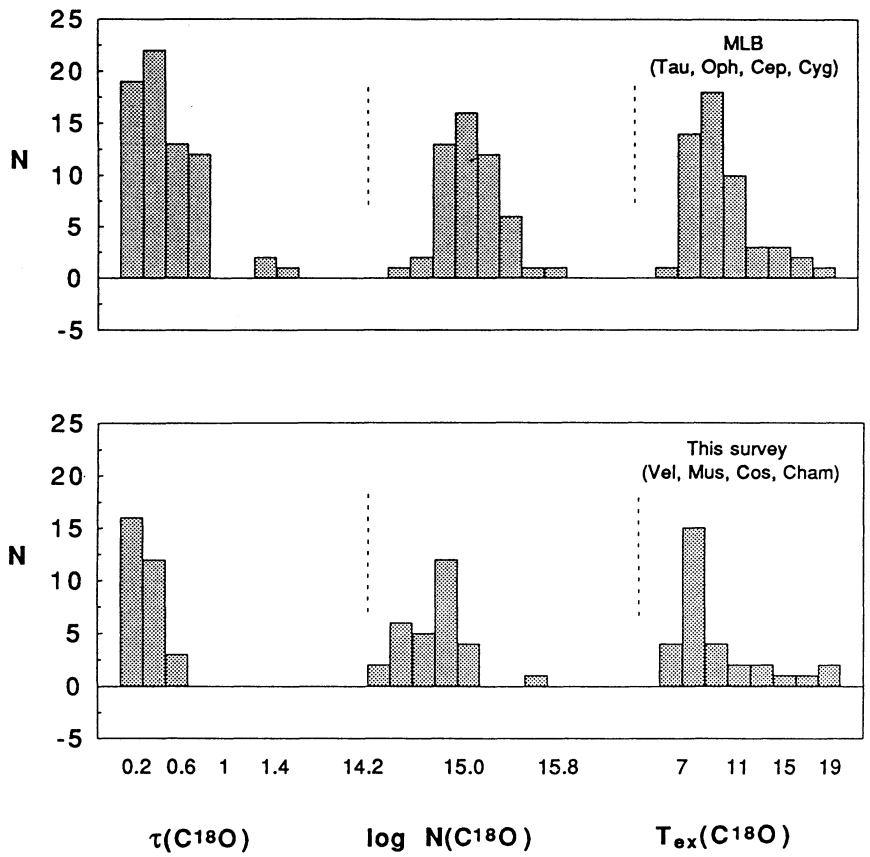

FIG. 5.—Histograms of the $C^{18}O$ optical depth, column density, and excitation temperatures observed by MLB and this survey. These histograms do not include τ_{18} and $N(C^{18}O)$ upper limits. The peak of the distribution observed in this survey suggest lower $C^{18}O$ optical depth, column density, and excitation temperatures than observed by MLB.

Drake (1978),

$$N(H_2) = 0.94 \times 10^{21} A_V \text{ cm}^{-2}, \quad (5)$$

where A_V is the visual extinction in magnitudes, which we estimated from $C^{18}O$ observations.

Our procedure was to use for each region the best-fit linear relation between $N(C^{18}O)$ and A_V derived from star counts, unless this relation is statistically indistinguishable from one already determined for another region.

In order to calculate $N(H_2)$ using the $C^{18}O$ observational results we used different relations between the visual extinction and the estimated $C^{18}O$ column density. Among the regions observed in this survey, Vela is the one where the condensations had their visual extinction determined from the Hartley et al. (1986) classification. Only three condensations observed in this region had been classified as class B, and the other 16 are class A. The class A extinction is defined by Hartley et al. (1986) as a region where no background stars is visible. This correspond to the regions with maximum visual extinction 6 mag as estimated by Hetem et al. (1988). Class B are sources with Lynds opacity 4 to 5, which corresponds approximately to the same interval of visual extinction estimated by star counts.

In order to plot $N(C^{18}O)$ versus visual extinction we assume the class A and B sources as having visual extinction 6 and 4.5, respectively. The result is shown in Figure 6*a*, where the relations $N(C^{18}O)$ versus A_V obtained by Cernicharo & Guelin (1987, hereafter CG), FLW and that one used by Nozawa et al. (1991, hereafter NMTOF) are represented by dotted lines. Although there is a big dispersion in the data for visual extinction 6, the relation used by NMTOF seems to be more appropriate to represent the data. Thus in order to estimate the column density of the condensations in Vela we used the following relation

$$A_V = 6.40 \times 10^{-15} N(C^{18}O) + 3.2 \text{ mag} \quad (6)$$

used by NMTOF for the Ophiuchus north region, and valid when the optical extinction is between 3 and 14 mag. This relation is appropriate for condensations which are under the action of a strong external ultraviolet radiation field (NMTOF).

For the Coalsack and Chamaeleon sources we used the relation

$$A_V = 6.2 \times 10^{-15} N(C^{18}O) + 1.4 \text{ mag} \quad (7)$$

obtained by Frerking, Langer, & Wilson (1982, hereafter FLW) for dense condensations in Taurus with $C^{18}O$ column densities greater than or equal to 3×10^{14} cm^{-2}, where the effects of saturation have been corrected by using $C^{17}O$ and $^{13}C^{18}O$ data. This relation seems to be appropriate for dense condensations in dark clouds which are not under the action of a strong UV radiation field. Figure 6*b* shows $N(C^{18}O)$ versus A_V obtained from Hetem et al. (1988) star counts for Chamaeleon sources. In this figure the FLW relation given by equation (7) is also shown. There is only one position where the $C^{18}O$ column density is very high compared to the average value observed;

TABLE 2

DERIVED PROPERTIES OF THE CONDENSATIONS

Source		RA (1950) (h, m, s)	DEC (1950) (deg, m, s)	Av [opt] (mag)	Optical Size l(>) (arc min)	Optical Size b(<) (arc min)	Dist. (pc)	L (pc)	Av [C18O] (mag)	N(H2) 1.E+21 (cm-2)	n(H2) 1.E+03 (cm-3)		Mmax (Mo)	Notes
1	V1	07 14 28	-43 52 18	4	4	2	300	0.25	4.7	4.4	5.7	>	5.9	1
2	V2	07 26 20	-50 58 18	6	16	2	300	0.49	6.8	6.4	4.2		34.7	1
3	V3	07 27 53	-41 04 12	6	6	1	300	0.21	4.1	3.8	5.8	>	3.9	1
4	V4	07 29 05	-46 37 18	4	8	2	300	0.35	4.2	3.9	3.6	>	10.6	1
5	V5	07 31 03	-50 39 06	6	14	2	300	0.46	4.6	4.3	3.1		20.6	1
6	V6	07 32 41	-46 47 42	4	22	7	300	1.08						1
7	V7	07 37 18	-49 43 48	6	12	2	300	0.43	5.0	4.7	3.6		19.0	1
8	V8	07 37 42	-47 46 12	6	7	2	300	0.33	5.1	4.8	4.8	>	11.4	1
9	V9	07 39 16	-43 42 06	6	4	1	300	0.17	4.7	4.4	8.2		3.0	1
10	V10	07 40 51	-41 58 00	6	4	1	300	0.17						1
11	V11	07 41 26	-42 00 18	6	2	1	300	0.12	4.0	3.8	9.9	>	1.3	1
12	V12	07 41 56	-42 14 48	6	2	1.5	300	0.15	3.7	3.4	7.4	>	1.7	1
13	V13	08 07 04	-35 50 30	6	7	3	300	0.40	3.9	3.7	3.0	>	13.1	1
14	V14	08 07 39	-35 55 54	6	3	2	300	0.21	9.8	9.2	13.9		9.3	1
15	V15	08 10 25	-33 47 12	6	3	1	300	0.15						1
16	V16	08 10 27	-33 51 60	6	5	1.2	300	0.21	4.6	4.3	6.6	>	4.4	1
17	V17	08 10 28	-33 36 36	6	4	2	300	0.25						1
18	V18	08 12 26	-34 21 42	6	10	1.5	300	0.34	7.6	7.1	6.8		18.0	1
19	V19	08 13 32	-33 55 30	6	6	1.6	300	0.27						1
20	V20	08 14 03	-33 41 30	6	7	1.2	300	0.25	6.0	5.7	7.3		8.0	1
21	V21	08 17 32	-42 45 18	6	5	2	300	0.28						1
22	V22	08 26 48	-33 35 48	6	65	6	300	1.72	5.1	4.8	0.9	>	316.5	1
23	V23	08 35 23	-36 27 24	6	6	2	300	0.30	4.2	4.0	4.3	>	8.1	1
24	V24	08 51 04	-50 28 42	6	2.5	0.5	300	0.10						1
25	V25	08 51 04	-51 40 30	6	3	1	300	0.15	3.9	3.7	7.9	>	1.9	1
26	V26	09 12 13	-42 17 36	6	12	1.5	300	0.37						1
27	V27	09 20 29	-45 36 00	6	14	4	300	0.65	8.2	7.7	3.8		72.7	1
28	Mu1	12 18 52	-72 05 25	3.2	6.7	4.5	225	0.36	1.8	1.7	1.6	>	5.0	2
29	Mu2	12 18 53	-71 44 50	2.2	4.5	4.5	225	0.29						2
30	Mu3	12 19 28	-71 51 57	2.6	6.7	4.5	225	0.36	2.2	2.1	1.9	>	6.0	2
31	Mu4	12 21 29	-71 35 56	3.6	9	4.5	225	0.42	4.6	4.3	3.3		16.5	2
32	Mu5	12 22 30	-71 24 38	3.9	9	6.7	225	0.51	6.1	5.7	3.7		32.9	2
33	Mu6	12 23 20	-71 09 60	3.2	6.7	6.6	225	0.44	1.8	1.7	1.3	>	7.3	2
34	Mu7	12 25 32	-71 02 44	3.3	9	6.7	225	0.51	3.8	3.6	2.3		20.4	2
35	Mu8	12 26 19	-70 54 13	2.7	4.5	4.5	225	0.29	4.1	3.8	4.2		7.4	2
36	Mu9	12 27 50	-70 54 01		5	2.5	225	0.23	4.9	4.6	6.5		5.5	
37	Mu10	12 27 57	-70 46 18	4.1	11	9	225	0.65	5.3	5.0	2.5		47.1	2
38	Mu11	12 28 42	-70 45 07		3.5	3.5	225	0.23	4.3	4.0	5.7		4.7	
39	Mu12	12 29 31	-70 28 55	6	6	2	225	0.23						1
40	Mu13	12 32 05	-70 24 15	2.5	6.7	4.5	225	0.36	1.8	1.7	1.5	>	4.7	2
								0.36	1.9	1.7	1.6			
41	Mu14	12 33 01	-69 52 45		2.5	2.5	225	0.16						
42	Mu15	12 33 15	-70 17 03		2.5	2	225	0.15	1.9	1.7	3.9	>	0.8	2
43	Mu16	12 34 24	-70 13 59	2	4.5	2.2	225	0.21						2
44	CoS1	12 19 21	-66 10 30	6	3	3	175	0.15	3.1	2.9	6.3		1.5	1
45	CoS2	12 28 28	-63 28 22	4.9	6.7	6.7	175	0.34	6.9	6.5	6.2		16.8	2
46	CoS3	12 30 12	-63 33 54	6	55	5	175	0.84	4.8	4.5	1.7		71.5	1
47	CoS4	12 30 57	-63 23 12	4.2	6.7	4.5	175	0.28	5.8	5.5	6.3		9.5	2
48	CoS5	12 40 12	-61 49 36	4	16	4	175	0.41	2.0	1.9	1.5	>	7.0	1
49	CoS6	12 55 27	-66 08 24	4	5	2	175	0.16						1
50	CoS7	12 55 51	-61 04 06	6	5	3	175	0.20	3.3	3.1	5.1		2.7	1
51	CoS8	13 09 02	-64 09 48	4	12	5	175	0.39						1
52	CoS9	13 09 07	-64 49 00	4	3	3	175	0.15						1
53	CoS10	13 15 31	-62 26 12	6	6	4	175	0.25						1
54	CoS11	13 16 05	-64 19 30	6	7	5	175	0.30						1
55	CoS12	13 16 15	-62 17 42	6	6	2	175	0.18						1

TABLE 2—*Continued*

Source		RA (1950) (h, m, s)	DEC (1950) (deg, m, s)	Av [opt] (mag)	Optical Size l(>) (arc min)	Optical Size b(<) (arc min)	Dist. (pc)	L (pc)	Av [C18O] (mag)	N(H2) 1.E+21 (cm-2)	n(H2) 1.E+03 (cm-3)		Mmax (Mo)	Notes
56	CoS13	13 17 00	-64 57 18	4	5	3	175	0.20						1
57	CoS14	13 21 31	-63 27 18	4	6	3	175	0.22						1
58	Cha1	12 44 15	-76 33 00	2.4	6.7	6.7	200	0.39						2
59	Cha2	12 45 23	-76 30 50		2	2	200	0.12						
60	Cha3	12 45 25	-77 05 24	2.4	4.5	4.5	200	0.26						2
61	Cha4	12 46 28	-76 35 60	4	9	9	200	0.52	3.5	3.3	2.0		19.9	1
62	Cha5	12 48 01	-76 37 01		3	2.5	200	0.16						
63	Cha6	12 48 12	-76 56 37	2.8	4.5	4.5	200	0.26						2
64	Cha7	12 49 47	-76 54 39		3.5	2.5	200	0.17	3.6	3.4	6.4		2.2	
								0.17	4.5	4.3	8.1			
65	Cha8	12 49 51	-76 47 24	5.1	13.5	11	200	0.71	4.4	4.1	1.9		46.3	2
66	Cha9	12 50 48	-76 18 35	2.8	4.5	4.5	200	0.26						
67	Cha10	12 51 08	-76 55 14		2.5	2.5	200	0.15						
68	Cha11	12 51 12	-76 29 30	2.4	9	2.2	200	0.26						2
69	Cha12	12 52 38	-76 34 30	2.4	6.7	2.2	200	0.22						2
70	Cha13	12 53 20	-77 12 00	2.9	7.7	4.5	200	0.34						2
71	Cha14	12 53 30	-76 22 60	2.4	4.5	4.5	200	0.26						2
72	Cha15	12 54 02	-75 51 27	2.4	9	6.7	200	0.45						2
73	Cha16	12 55 16	-77 12 20		9	4.5	200	0.37	2.7	2.5	2.2	>	7.6	2
74	Cha17	12 56 14	-77 00 00		2.5	2	200	0.13	6.8	6.4	16.0		2.4	
75	Cha18	12 56 20	-76 55 26	5.5	15.4	14	200	0.85	7.4	7.0	2.7		113.3	2
76	Cha19	12 57 45	-77 01 10		2	2	200	0.12	7.4	7.0	19.5		2.1	
77	Cha20	12 59 06	-77 06 20		4	2	200	0.16	6.0	5.6	11.1		3.4	
78	Cha21	12 59 23	-77 23 50	4.5	11	9	200	0.58						2
79	Cha22	12 59 53	-77 42 45	3.7	6.7	4.5	200	0.32						2
80	Cha23	13 00 26	-77 05 24	3.8	9	9	200	0.52						2
81	Cha24	13 01 21	-77 36 47		3.5	2.5	200	0.17	1.9	1.8	3.4	>	1.2	
82	Cha25	13 02 00	-77 48 07		4.5	4	200	0.25						
83	Cha26	13 03 18	-76 45 50	2.4	6.7	6.7	200	0.39						2
84	Cha27	13 03 20	-77 26 60	4.4	9	9	200	0.52						2
85	Cha28	13 03 46	-77 43 45	3.7	4.5	2.2	200	0.18						2
86	Cha29	12 22 25	-79 06 60	3.3	9	4.5	200	0.37	8.9	8.4	7.3		25.4	2
87	Cha30	12 23 27	-80 08 38	4.3	13.5	6.7	200	0.55	2.5	2.3	1.4	>	15.7	2
88	Cha31	12 29 30	-80 17 60	3.2	4.5	4.5	200	0.26						2
89	Cha32	12 32 00	-80 15 39	3.8	11.2	4.5	200	0.41						2
90	Cha33	12 37 50	-79 57 60	3.4	6.7	4.5	200	0.32						2
91	Cha34	12 40 10	-79 43 00	3.1	4.5	4.5	200	0.26						2
92	Cha35	12 40 40	-79 59 00	3.4	6.7	4.5	200	0.32	3.7	3.5	3.5		7.8	2
93	Cha36	12 41 15	-80 12 40	3.4	6.7	4.5	200	0.32	4.1	3.8	3.9	>	8.7	2
94	Cha37	12 49 20	-79 42 00	3.1	4.5	2.2	200	0.18	3.4	3.2	5.7		2.4	2
95	Cha38	12 49 37	-79 06 45	3.3	4.5	4.5	200	0.26						2
96	Cha39	12 50 22	-79 17 60	4.9	6.7	6.7	200	0.39	3.3	3.1	2.5	>	10.3	2
									2.0	1.8				
97	Cha40	12 50 52	-79 11 15	4.9	6.7	6.7	200	0.39						2
98	Cha41	12 51 00	-79 29 00	4.6	4.5	4.5	200	0.26						2
99	Cha42	12 52 55	-78 40 00	4	9	6.7	200	0.45						2
100	Cha43	12 53 00	-78 51 27	3.4	6.7	2.2	200	0.22						2
101	Cha44	12 53 00	-79 01 07	3.3	6.7	4.5	200	0.32						2

NOTES.—(1) The opacity is obtained from Hartley et al. 1986; (2) the opacity is obtained from Hetem et al. 1988 and the size is defined by a contour of 2 magnitudes visual extinction. The distance to the clouds were obtained from Harju et al. 1991 (Vela), Hetem et al. 1988 (Musca), Rogers 1960 (Coalsack), Gauvin & Strom 1992 (Chamaeleon II and III).

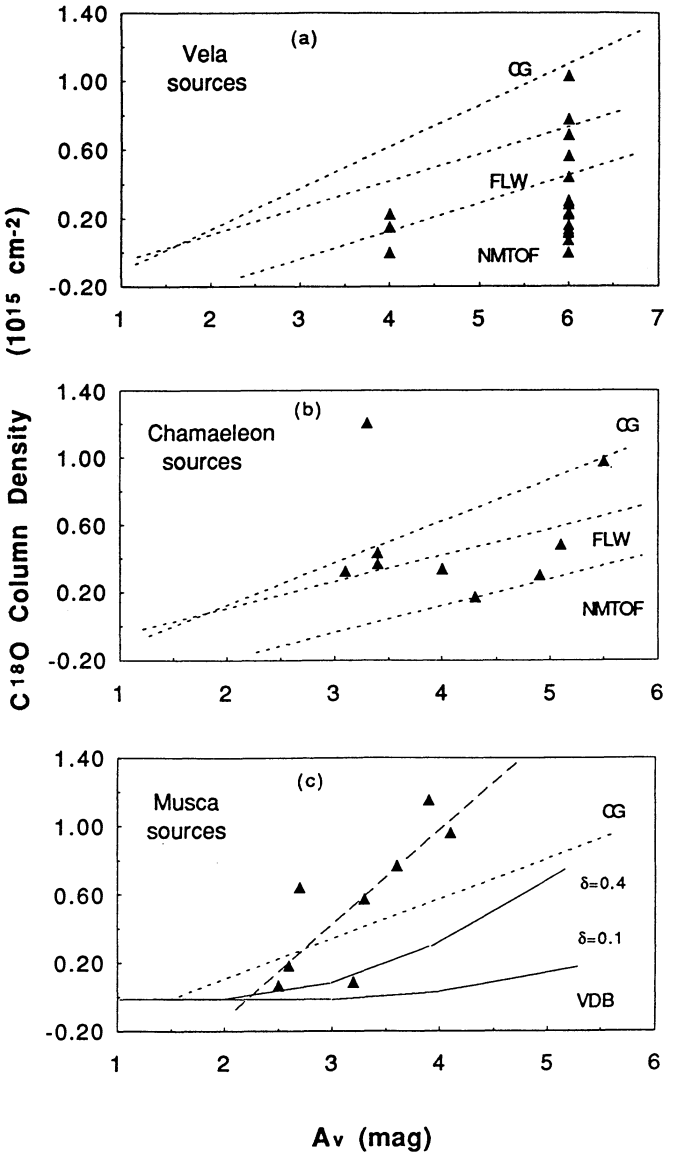

FIG. 6.—The observed $C^{18}O$ column densities, indicated by filled triangles, vs. visual extinction for Vela, Chamaeleon, and Musca. The visual extinction in Vela was estimated from Hartley et al. (1986). In Chamaeleon and Musca they were obtained from Hetem et al. (1988). The dotted lines are column density vs. extinction obtained in different clouds by Cernicharo & Guelin (1987) (CG), Frerking, Langer, & Wilson (1982) (FLW), and Nozawa et al. (1991) (NMTOF). Only for Musca, the Van Dishoeck & Black (1988) (VDB) models are plotted where the radiation field of Draine (1978) is adopted. In Musca, the upper and lower solid lines are models with carbon depletion 0.4 and 0.1, respectively, and the dashed line is the best linear regression fit to the data.

the other positions have column densities that follow approximately equation (7) above.

Figure 6*c* shows the data obtained for the Musca sources, where the positions with column densities lower than 0.2×10^{15} cm^{-2} are lower limits. For this cloud we used the column densities versus visual extinction relation,

$$A_V = 1.8 \times 10^{-15} N(C^{18}) + 2.2 \text{ mag}, \quad (8)$$

obtained by a linear fit of the data. This line is represented in Figure 6*c* by a dashed line. A relation similar to this one was observed by Cernicharo & Guelin (1987) in Heiles's cloud 2 (represented by a dotted line in the same figure).

In Figures 6*c* the solid lines are theoretical models derived by Van Dishoeck & Black (1988, hereafter VDB) for clouds with extinction values spanning the typical range of diffuse and dense clouds (A_V = 1–5 mag) under the action of a normal ultraviolet radiation field (the interstellar radiation field, as suggested by Draine 1978). The upper and lower lines are cloud models with carbon depletion 0.4 and 0.1, respectively. In all these models there are gradients of temperature and density through the clouds (VDB). For the same carbon depletion, if the external radiation field is enhanced, lower values of column densities are obtained.

Musca resembles the streamers L1506 in Taurus and L1755 in Ophiuchus, in its extinction, its low incidence of young stars, and in its apparently normal interstellar radiation field. Yet the VDB models fail to account for the estimated $C^{18}O$ column densities in Musca. Similar results were obtained by CG for Heiles 2 cloud. In this case VDB suggest that the high $C^{18}O$ column density could be explained if the volume density in the observed positions is higher than 10^4 cm^{-3} or if the external radiation field is significantly weaker than the normal field.

6.2. *Molecular Volume Density and Mass of the Condensations*

To estimate the molecular hydrogen volume density we used $N(H_2)$ column densities and the optical size of the condensation as defined in § 2. The condensations are assumed to be uniform spheres of gas-and-dust with average densities given by

$$n(H_2) = N(H_2)/L, \quad (9)$$

where L is the optical size of the condensation. As pointed out by MLB, the volume density obtained by using this equation is an upper limit since the visual extinction used to estimate the column density is integrated along the entire line of sight instead of just along the condensation. This is particularly important when the observed condensations are embedded in an extended cloud, as is the case of almost all condensations observed in dark clouds. However, this seems not to be the case for the condensations observed in Vela, where the density of intercondensation gas is evidently much lower than in extended dark clouds.

The corresponding maximum mass of the condensations was estimated from the uniform sphere model, using the equation

$$M = 22.2 \left[\frac{N(H_2)}{10^{21} \text{ cm}^{-2}} \right] \left(\frac{L}{\text{pc}} \right)^2 M_\odot, \quad (10)$$

where L is the diameter of the condensation. The mass is uncertain at least by a factor of 2.5 due to the uncertainties in the source distances and in the factor to convert from $C^{18}O$ column density to $N(H_2)$.

These parameters are given in Table 2 for all observed positions. The masses indicated as lower limit are positions where the ^{13}CO to $C^{18}O$ antenna temperature ratio is high (> 7) and the $C^{18}O$ optical depth, according to the model used, is a lower limit.

Table 3 gives the average values of the derived parameters. In column (1) is given the source name, columns (2), (3), and (4) give the average value of the optical size, volume density, and mass for all condensations observed in each cloud. The rms dispersion of each parameter are given in brackets attached to the average values. The lines in bold type means that the parameter was estimated using all data even if it is a limit. Normal type means that the limits are not considered. These parameters were estimated from Table 2.

TABLE 3

AVERAGE VALUES OF CONDENSATION SIZE, DENSITY, AND MASS

Source	L (pc)	$n(H_2)$ (10^3 cm^{-3})	M ($M_\odot$)
Vela	**0.4 (0.3)**	**6 (3)**	**30 (71)**
	0.4 (0.2)	6 (4)	24 (22)
Musca	**0.3 (0.1)**	**3 (2)**	**13 (14)**
	0.3	4.0	19
Coalsack	**0.3**	**4.5**	**18**
	0.3	5.1	20
Chamaeleon II	**0.3**	**7.0**	**22**
	0.3	8.6	27
Chamaeleon III	**0.3**	**4.0**	**12**
	0.4	5.5	12

NOTE.—The rms of the average values which were estimated from Table 2 of this paper are given in parentheses. In bold type are the averages estimated using all measurements (including limits), the rms value of the parameters are given in parentheses.

Only in V14 the volume density (1.4×10^4 cm^{-3}) is a factor of 2 higher than the average density of the condensations observed in these clouds. Volume densities as high as this one have been also observed in Cha 17, Cha 18, and Cha 19. The highest average condensation masses were estimated for Chamaeleon II and Vela, while for Chamaeleon III masses lower by a factor of 2 are obtained.

6.3. *Properties of the Clouds Observed by MLB and This Survey*

In order to compare the properties of the clouds observed in this survey with those observed by MLB, only the line widths, excitation temperature, and column densities are compared. Other parameters like volume density and masses are not considered, since they are more uncertain than the previous ones. In order to make this comparison, the MLB data were separated by cloud and the average value of the selected parameters in each cloud were estimated. These values are shown in Table 4, where column (1) gives the cloud name; column (2), the number of condensations observed in ^{13}CO and C^{18}O; columns (3) and (4), the average value of the ^{13}CO and C^{18}O line widths; and columns (5), (6), and (7) give the averaged C^{18}O column density, excitation temperature, and H_2 column densities.

A few remarkable results are obtained comparing the data for these different clouds: (1) the highest ^{13}CO line widths are observed in Ophiuchus (1.9 km s^{-1}), and the smallest ones, $\sim$3 times narrower, are observed in Vela (0.7 km s^{-1}). For the same clouds the C^{18}O line widths differ by less than 34%, suggesting that the mechanism responsible for the ^{13}CO line broadening does not similarly affect the C^{18}O. The narrow ^{13}CO line width observed in Vela could be a consequence of the existence of a tenuous intercondensation gas, which does not contribute to the emission produced in the densest part of the condensation. This negligible intercondensation gas may reduce the source of turbulence in the cloud. Narrow ^{13}CO line widths are also observed in Coalsack and Musca. (2) From cloud to cloud, the C^{18}O line width is almost constant and again seems not to be affected by the same mechanism that produces the ^{13}CO line broadening. (3) The highest C^{18}O column density is estimated for Ophiuchus (2.6×10^{15} cm^{-2}) and gets smaller as we go to Taurus, Cepheus, and the other clouds observed in this survey. In Taurus, Ophiuchus, and Cepheus the C^{18}O column densities are higher by at least a factor of 2 than estimated for Vela, Musca, Coalsack, and Chamaeleon clouds. Since the condensations observed in these clouds have almost the same average sizes (Table 3), the high column densities suggest that in Ophiuchus the condensations are on average 2 times denser than in Taurus and Cepheus and 4 times denser than in the other clouds. (4) The highest average excitation temperature was estimated for Ophiuchus (14 K) and the smallest for Chamaeleon clouds (7 K). Comparing the excitation temperature estimated for Ophiuchus, Taurus, Cepheus, Vela, Musca, and Coalsack, we can conclude that it is almost constant even if the column density changes by a factor of 4, or if the ^{13}CO line width changes by a factor of 2. Only comparing Ophiuchus with Chamaeleon clouds it seem that the excitation temperature changes by a factor of 2 when the column density changes by 4. This trend is not observed in the other clouds.

A search for *IRAS* sources associated with these clouds (Beichmann et al. 1986) indicates that more than 37% of the positions observed by MLB in Ophiuchus, Taurus, and Perseus have an infrared source associated. The clouds observed in this survey, as discussed in the next topic, have less than 10% of the condensations associated with an *IRAS* source, suggesting that the clouds observed by MLB are places where the star formation is more active. Among the parameters listed in Table 4, the high column densities seem to be the unique clear indicator of this activity.

TABLE 4

AVERAGE VALUES OF CONDENSATION LINE WIDTH, COLUMN DENSITY, AND EXCITATION TEMPERATURE OBTAINED BY MLB AND THIS SURVEY

Cloud	Number of Condensations ^{13}CO/C^{18}O	$\Delta V(^{13}$CO) (km/s)	ΔV(C^{18}O) (km/s)	N_{18} (1E15 cm^{-2})	T_{ex} (K)	$N(H_2)$ (1E21 cm^{-2})
Taurus	26/26	1.0 (0.3)	0.6 (0.2)	1.6 (1.0)	10 (2)	10 (6)
Ophiuchus	14/14	1.9 (1.0)	0.8 (0.4)	2.6 (2.0)	14 (3)	14 (10)
Cepheus	06/06	1.3 (0.4)	0.6 (0.2)	1.1 (0.5)	9 (2)	7 (2)
Vela	26/19	0.7 (0.2)	0.6 (0.2)	0.5 (0.3)	12 (2)	6 (2)
Musca	16/13	0.8 (0.2)	0.5 (0.1)	0.8 (0.2)	10 (4)	4 (1)
Coalsack	14/06	0.8 (0.2)	0.5 (0.1)	0.6 (0.3)	11 (4)	5 (2)
Cham II	28/11	1.2 (0.4)	0.7 (0.3)	0.7 (0.3)	7 (2)	5 (2)
Cham III	13/08	1.1 (0.3)	0.9 (0.5)	0.6 (0.5)	7 (1)	3 (1)

NOTE.—The values given in this table are the average of the parameter obtained for each cloud estimated from Table 1 of this survey and Table 3 from MLB. The rms value for these parameters are given in parentheses.

The results given in Figure 5 and Table 4 show that the condensations observed in this survey have column densities smaller than observed by MLB in Taurus, Cepheus, and Ophiuchus. In order to verify if this result is related to total density of the condensations or to different ^{13}CO and $C^{18}O$ abundances, 19 condensations observed by MLB with visual extinction estimated by Cernicharo & Bachiller (1984) were selected to compare their visual extinction distribution with the extinction distribution of the sources observed in this survey. No systematic difference is expected between the visual extinctions obtained by Hetem et al. (1988) and Cernicharo & Bachiller (1984) since they used rectilinear grids with 2.2 resolution to make star counts, and the same equation was used to obtain the visual extinction from blue extinction. Hetem et al. (1988) made counts on the ESO B plates and Cernicharo & Bachiller (1984) on the blue and red Palomar Observatory Sky Survey (POSS) prints.

The histogram of the extinction distribution is shown in Figure 7. The peak of the distribution for the MLB condensations is shifted by 1 mag to higher visual extinction than the condensations observed in this survey. This distribution also suggests that there are more condensations with visual extinction higher than 4 mag in the MLB survey than in this survey. This result corroborates the conclusion in Table 4 that the condensations observed in this survey are less massive than those observed by MLB. We show in § 8.4 that the low-extinction cores tend to have relatively few associated young stars, while the higher extinction cores observed by MLB tend to have more associated young stars.

7. *IRAS* SOURCES AND YOUNG STELLAR OBJECTS

A search for infrared sources and young stellar objects was conducted using the *IRAS* Point Source Catalog (Beichman et al. 1984) and surveys of T Tauri and pre–main-sequence emission-line stars (Schwartz 1977; Whittet, Prust, & Wesselius 1991; Weintraub 1990; Herbing & Bell 1988; Gauvin & Strom 1992; Persi et al. 1990).

Initially, we selected all *IRAS* sources located less than 15′ from the condensation position, with at least two contiguous *IRAS* bands having flux quality higher or equal to 2. This criterion eliminates sources detected only in 100 μm although some sources detected only at these wavelength are correlated with cloud condensations (Beichman et al. 1986). A total of 185 sources were thereby selected. In order to select the *IRAS* sources candidates to pre–main-Sequence Stars (PMS) a constraint was imposed on the infrared properties of the sources to exclude from the sample ordinary stars: all sources with spectral slopes

$$\alpha_{12} = \log [\nu_{12} F_{12}/\nu_{25} F_{25}]/\log [\nu_{12}/\nu_{25}] ,$$
$$\alpha_{25} = \log [\nu_{25} F_{25}/\nu_{60} F_{60}]/\log [\nu_{25}/\nu_{60}] , \qquad (11)$$

in the interval $-2.0 < \alpha_{12} < 1.35$ and $-1.75 < \alpha_{25} < 2.2$ were selected. This constraint defines the spectral slope interval for almost all known PMS emission-line stars (Weintraub 1990). In this interval are contained similar criteria used by Beichman et al. (1986), Harris (1985), and Harris, Clegg, & Hughes (1988) to identify PMS stars. A total of 56 sources satisfies the criteria given by the equation (11). Finally, in order to establish the association of the *IRAS* sources with the condensations we selected all *IRAS* sources located at a distance from the condensation position less than the smaller optical size of the condensation. This criterion is essentially the same as that used by Beichman et al. (1986) to analyze the results of MLB.

This constraint is satisfied by only eight *IRAS* sources, which are reduced to six when sources in confused fields are eliminated due to cirrus clouds or point sources. This information was obtained using various data quality indicators in the *IRAS* Point Source Catalog. These sources are listed in Table 5, which gives the name of the condensation and its respective

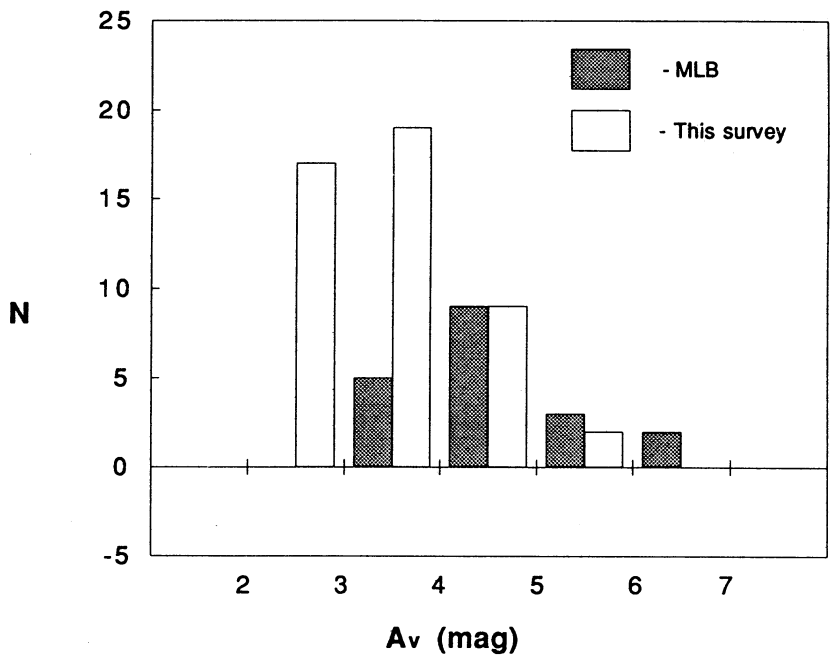

FIG. 7.—Histogram of the distribution of visual extinction based on star counts for 19 condensations observed by MLB and for 47 observed in this survey

1994ApJ...433...96V

TABLE 5

DERIVED PROPERTIES OF THE *IRAS* SOURCES

CORE	IRAS SOURCE	Uncorrected Flux Density in Jansky				Color Temperature in K			IR-Pos. (pc)	L(IRAS) Lo	Association	Ref.	Note
		12	25	60	100	T12	T25	T60					
V6(3)	07329-4647	0.25	0.38 [0.02]	1.33 [0.13]	5.62	-	87	-	0.22	0.91			
V14(2)	08076-3556	0.63 [0.10]	3.75 [0.19]	18.00 [1.98]	46.70 [4.70]	158	81	39	0.03	7.07	HBC554,555	3,4	CI
V22(1)	08267-3336	0.40 [0.02]	1.10 [0.07]	3.17 [0.25]	13.90 [1.25]	195	92	32	0.09	2.16	HBC562	3,5	TT
Mu13(2)	12322-7023	3.44 [0.38]	8.96 [0.45]	12.60 [1.01]	11.40 [1.82]	200	118	72	0.08	4.18		1	TT?
Cha8(1)	12496-7650	39.40 [1.58]	85.60 [6.00]	104.00 [10.4]	86.10 [14.0]	215	125	80	0.21	32.00	DC303.0-14.3	1,2	CI
Cha18(1)	12553-7651	0.62 [0.04]	3.86 [0.23]	9.52 [0.86]	10.40	155	95	62	0.28	1.61	DC303.4-14.3	1,2	
	12571-7654	0.31	0.59 [0.21]	0.86 [0.15]	5.63 [1.52]	-	117	28	0.16	0.50	Sz50	1,2	TT?

NOTES.—TT = T Tauri type star; TT? = T Tauri Candidate; CI = Class I source (Lada & Wilking 1984); 1 = Hetem et al. 1988; 2 = Gauvin & Strom 1992; 3 = Herbig & Bell 1988; 4 = Persi et al. 1990; 5 = Weintraub 1990. The flux density uncertainties are given in brackets.

associated *IRAS* source, the uncorrected flux density in Janskys at the four *IRAS* bands, the color temperature, the distance of the infrared source from the center of the condensation position in parsecs, the infrared luminosity of the source in solar luminosities, and the name of the associated object. Also the last two columns give references and notes about the associated object. Attached to the name of the condensation is given, between commas, the number of *IRAS* point sources which had flux quality higher than 1 in only one *IRAS* band and which are less than 15′ from the condensation position. For all infrared sources the point source correlation coefficient is higher than 97% in the bands with flux quality higher or equal to 2. Attached to the flux densities are given the flux uncertainties; when this parameter is not given, the flux densities are upper limits.

There is a remarkable difference between the number of condensations with *IRAS* sources observed in MLB and this survey. While in MLB almost 50% of the observed condensations have *IRAS* sources associated, in this survey only 8% of the condensations have *IRAS* sources. This is an indication that the condensations observed in this survey are in regions of low star formation activity. A similar result was obtained by Persi et al. (1990), who searched 482 southern dark clouds and found evidence of young stellar objects associated with 6% of these clouds.

The color temperatures are estimated using the flux density ratios from different frequency bands. Bands where the flux density are limits were not considered. The luminosity was calculated integrating $\Omega_{12} B(\nu, T_{12}) + \Omega_{60} B(\nu, T_{60})$ over all wavelengths, assuming that the emission in the frequencies band 12–25 μm and 60–100 μm are produced by distinct regions with temperatures T_{12} and T_{60} and solid angle Ω_{12} and Ω_{60}, respectively. This method was used in 20 *IRAS* sources, whose *IRAS* luminosity was determined by integrating their flux density over four *IRAS* bands (Beichman et al. 1986), and whose bolometric luminosity was estimated by integrating over several photometric bands between 0.4 and 100 μm (Myers et al. 1987). Except for one source, the method used here gives luminosities which are closer to the bolometric one than to that obtained by integrating over the 4 *IRAS* bands and making the long-wavelength bolometric correction.

Among the *IRAS* sources in Table 5, one is a T Tauri star, two are candidate T Tauri stars, and two are class I sources as defined by Lada & Wilking 1984).

8. INDIVIDUAL REGIONS

In this section we will discuss some relevant aspects of the clouds observed in this survey, except the Coalsack region where only few condensations have been observed.

8.1. *Vela: Velocities*

The Vela condensations observed in this survey span a much wider range of position in the sky than do condensations in most molecular cloud complexes. The radial velocity of the condensations observed in this region spans a velocity interval of 20 km s^{-1} which is at least 5 times wider than the range of radial velocities observed toward other clouds in this survey. The radial velocity dispersion, defined here as the standard deviation of the observed radial velocities, is $\sim$4.6 km s^{-1} for the Vela condensations. This high-velocity dispersion is compatible with the scenario proposed by Reipurth (1983). In this picture, the globules are surviving condensations of a molecular cloud which was disrupted by the action of a powerful internal energy source.

If we adopt this scenario and assume that 5% of the original cloud mass was in condensations with density substantially above the mean (Falgarone & Puget 1986), we estimated a lower limit for the mass of the undisrupted Vela cloud as 6000 $M_\odot$ since the total mass of the condensations observed in this survey is higher than 300 $M_\odot$.

If we assume a velocity dispersion of 0.6 km s^{-1} or less for the unperturbed initial cloud, as observed in the other dark clouds of this survey, and the mass estimated above as the mass of the original Vela cloud we find that the energy required to change the initial velocity dispersion to 5 km s^{-1} must be higher than 10^{48} ergs. This energy was estimated using $\Delta W(\text{ergs}) = 5.9 \times 10^{43}\ M(M_\odot)[\Delta V_f^2 - \Delta V_i^2](\text{km s}^{-1})$ obtained from the virial equation neglecting the external pressure and magnetic field. The subscript f and i attached to velocity dispersion means final and initial, and M is the mass of the cloud in solar mass units. This equation gives a lower limit because only a fraction of the energy liberated by the source is converted in expansion motion, and we are assuming the mass of the cloud as estimated above.

These cometary globules are distributed in space forming a ring or a shell around γ Velorum, ζ Puppis, and the Vela supernova remanent (Zealey et al. 1983).

Formaldehyde observations toward nine of these globules (Zealey et al. 1983; Goss et al. 1980) suggest radial velocity (Zealey et al. 1983) dispersion, which is in agreement with the ^{13}CO data observed in the same CGs. However, the ^{13}CO velocity dispersion is higher by at least a factor of 2 when all the 26 observed positions are considered.

Detailed observations of these globules, as done by Harju et al. (1990), are still necessary to understand the condensations and their kinematics.

8.2. *Vela: Line Widths*

Although the Vela-Gum cometary globules have properties similar to dense condensations in dark clouds, they are located in regions very different from the dark cloud environment. As discussed in the previous section, these condensations are under the action of the wind and the far ultraviolet radiation field of a massive star that tend to remove all intercondensation gas leaving only the "naked" dense condensations (Reipurth 1983). A consequence of this mechanism is that the sizes of the emission regions in ^{13}CO and C^{18}O must be nearly the same, since there is relatively little intercondensation gas, and an abrupt density change must occur between the condensation and the intercondensation medium. Even the cometary globules with a very long tail, like CG1 where a small halo must be formed, the ^{13}CO and C^{18}O emission distribution has the same size scale in the head of the globule (Harju et al. 1990). In such situation, where the observed lines are optically thin, the ^{13}CO and C^{18}O line widths should be approximately equal if both lines are excited under the same physical conditions. In fact, the line width ratio observed in this cloud are closer to one than for the other clouds, as shown in Figure 4.

Small differences in these line widths must be expected due to the presence of cometary tail, which can hide the head of the globule depending on its orientation, or of a small halo formed by the globule mass loss.

Although more detailed observation of these globules are still necessary to clarify these points, the trend for C^{18}O to ^{13}CO line-width ratio close to one in these cometary globules

suggest that the smaller line-width ratio observed toward dense condensations in dense dark clouds could be a consequence of a more extended and turbulent cloud where the ^{13}CO emission is dominant compared to $C^{18}O$.

Although the signal-to-noise ratio for the $C^{18}O$ line is ~ 10, maps of these condensations at these transitions are still required to establish whether or not the observed line-width ratio is greater than 1.

8.3. *Musca: Velocities and Structure*

The Musca and Chamaeleon clouds form a set of clouds with Galactic longitude between 295° through 305° and Galactic latitude between −5° through −20° approximately located at the same distance (Hetem et al. 1988). The optical obscuration in Musca is a single elongated filament, almost perpendicular to the Galactic plane, with 3° length and less than 20 arc minutes wide.

Figure 8 shows the radial velocity versus position measured along this filament. Since all condensations in this cloud lie nearly along the same line in the plane of the sky, the position θ is defined as the angular distance between a condensation and the reference position, which is the position of the condensation with the smallest Galactic latitude. Only in the reference position, indicated by distance 0°, the spectrum shows two lines with radial velocities shifted ~ 1 km s^{-1} from the velocities observed in the closest positions (10′ away). Nonetheless, the spectra do not show wings. Mapping this condensation may reveal whether these lines are due to expansion (contraction) or superposition of different clouds with different radial velocities.

The visual extinction distribution in Musca (Fig. 10 of Hetem et al. 1988) suggests that this cloud is formed by one extended condensation with $A_V > 1$ where almost all positions observed on this survey are located, and one small apparently independent condensation 17′ in size where the observed ^{13}CO and $C^{18}O$ line profiles are double. According to the radial velocity distribution, the center and the borders of the biggest filament are moving with different radial velocities: from positions 10 through 95 the radial velocity gradient is 0.1 km s^{-1} pc^{-1}, while it is −0.1 km s^{-1} pc^{-1} from 106 through 135. Small deviations from a uniform velocity gradient are observed for the distance 60 and 90, where the local maximum suggests that there is a more local velocity distribution in these positions.

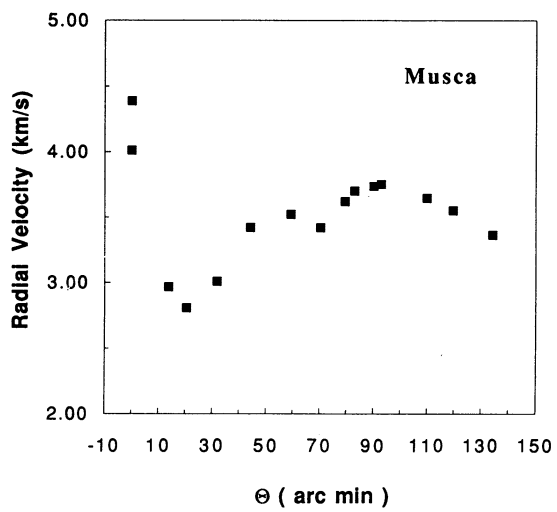

FIG. 8.—Radial velocity-position diagram for the condensations observed in Musca.

Filaments optically similar to Musca with velocity gradient of 0.11, and 0.26 km s^{-1} pc^{-1} have been observed in the Taurus filamentary structure, which includes Barnard 18 (Murphy & Myers 1985), and around the periphery of the Sharpless region S125 (McCutcheon, Roger, & Dickman 1982), respectively. Even these filaments are different from Musca because they are in a region with a more complex filamentary structure. In Taurus, the observed velocity gradients are probably due to a mild rotation of a more extended filament while in S125, where there are embedded protostars of spectral type B, rotation is considered as a possible cause for the extended geometry of the source (McCutcheon et al. 1982). The Musca filament is isolated, extending almost perpendicular to the Galactic plane, and there is only one candidate low-mass T Tauri star associated with this cloud (Table 5).

A simple analysis of the visual extinction distribution obtained by Hetem et al. (1988) in this cloud seems to be compatible with the hypothesis that its extent along the line of sight is about the same as its projected thickness in the plane of the sky. For cylinders with uniform density, the column density falls to 40% of its central value only when the distance to the center of the filament is 90% of the cylinder radius. These values seems to be in good agreement with the extinction maps, where the optical extinction seems to change appreciably only very close to the border of the cloud. Furthermore, the high aspect ratio, ~ 10, of the projected cloud makes it statistically much more likely to be prolate (cylindrical) than oblate (sheetlike) (e.g., Myers et al. 1991).

8.4. *Musca: Equilibrium*

An isothermal and self-gravitating, cylindrical cloud has mass per length given by $M/L = 2kT/\mu m_0 G$, obtained from models of self-gravitating polytropic and isothermal cylinders (Ostriker 1964), where T is temperature, μm_0 is the mean molecular mass which is given by 1.4 $m(H_2)$ (assuming one He for every five H_2) and G is the gravitational constant. In this model magnetic field is neglected, and there is no external pressure. Assuming that the support of the cloud is due to thermal and turbulent motions, we find $T = T_D = 161$ K, which is obtained from the average $C^{18}O$ line width observed in this cloud (Table 4). Using this temperature in the equation above, we obtain 30 $M_\odot$ pc^{-1} as the mass that Musca should have to be a self-gravitating cylinder. Assuming 253 $M_\odot$ as the total mass of Musca obtained from Hetem et al. (1988) extinction maps, and 10 pc as the length of the cloud, assuming that it is located at 200 pc of distance, we estimate 24 $M_\odot$ pc^{-1} as the total mass per unit length for the Musca cloud. This mass density suggests that this cloud is self-gravitating since the mass is uncertain by factor of 2.5. On the other hand, if the linear mass density is actually smaller than 30 $M_\odot$ pc^{-1} the cloud is not bounded, and it should disperse.

If the radial velocity differences observed along the bigger size of the filament (1 km s^{-1}) also occur in directions perpendicular to line of the sight, and if the cylinder is not bound, the apparent alignment of the filament indicates that it must be less than 2×10^5 yr old, which is the time to shift different parts of the cloud by 15′ (width of cloud) if they are moving with a velocity difference of 1 km s^{-1}. More detailed maps of this cloud are necessary to better understand the structure and dynamics of this filament.

8.5. *Chamaeleon II and III*

These clouds together with Chamaeleon I are spatially distributed, forming a kind of "head" for the Musca cloud (Fig. 3 in Feitzinger & Stuwe 1984). From the visual extinction distribution in these clouds (Hetem et al. 1988), we can conclude that Chamaeleon III has 3 times more condensations than Chamaeleon II. Only 25% of the condensations in Chamaeleon III with extinction higher than 2 mag have smaller structures inside with extinction higher or equal to 3 mag. This fraction is 62% and 45% for Chamaeleon I and Chamaeleon II, respectively, and the masses of the condensations decrease as we go from Chamaeleon I to Chamaeleon III. A similar result is obtained from our ^{13}CO and $C^{18}O$ observations Chamaeleon II and III. There, we found that although the selected condensations have almost the same projected optical size and line widths, their average mass is 3 times bigger in Chamaeleon II than Chamaeleon III.

In spite of the big number of condensations identified in Chamaeleon III only a small number were observed in ^{13}CO and $C^{18}O$ because of its small average visual extinction.

In Chamaeleon III, only Cha 39, the position with the highest visual extinction, showed ^{13}CO and $C^{18}O$ line profile split (as in Fig. 3). Although it seems to be superposition of two independent components, more detailed observations of this position are still required to understand what is causing this splitting.

Careful analysis of the radial velocity versus position for both clouds suggest almost constant velocity for Chamaeleon II (Fig. 9) and a velocity gradient lower than 0.1 km s^{-1} pc^{-1} in Chamaeleon III (Fig. 10) along the declination axis. The ^{13}CO and $C^{18}O$ radial velocities observed in these clouds indicate rms velocities dispersion of 0.64 km s^{-1} and 0.55 km s^{-1} for Chamaeleon II and Chamaeleon III, respectively.

Assuming spherical geometry for these clouds, and neglecting the external pressure and magnetic field, the virial mass can be obtained from $M(M_\odot) = 1.2 \times 10^3\ R(\mathrm{pc})\ \Delta V^2_{\mathrm{rms}}(\mathrm{km\ s^{-1}})$, where R is the cloud radius and ΔV_{rms} is the rms radial velocity dispersion estimated from the observed radial velocities (Table 1). Assuming the sizes of Chamaeleon II and Chamaeleon III as 2°.3 and 3°.1 (estimated from the extinction maps) and the velocity dispersion given above, the virial masses for both clouds are $1.7 \times 10^3\ M_\odot$ and $2 \times 10^3\ M_\odot$, respectively. The total mass of each clouds estimated from extinction maps (Hetem et al. 1988) is $2 \times 10^3\ M_\odot$. Considering that their mass are uncertain by at least a factor of 2.5, it seems that they are close to virial equilibrium.

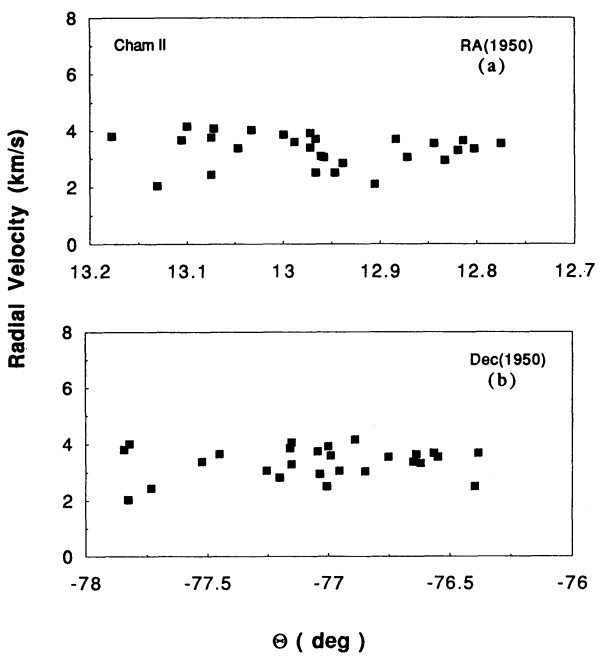

FIG. 9.—Radial velocity-position diagram for the condensations observed in Chamaeleon II cloud. In (*a*) and (*b*) the positions are right ascension and declination, respectively.

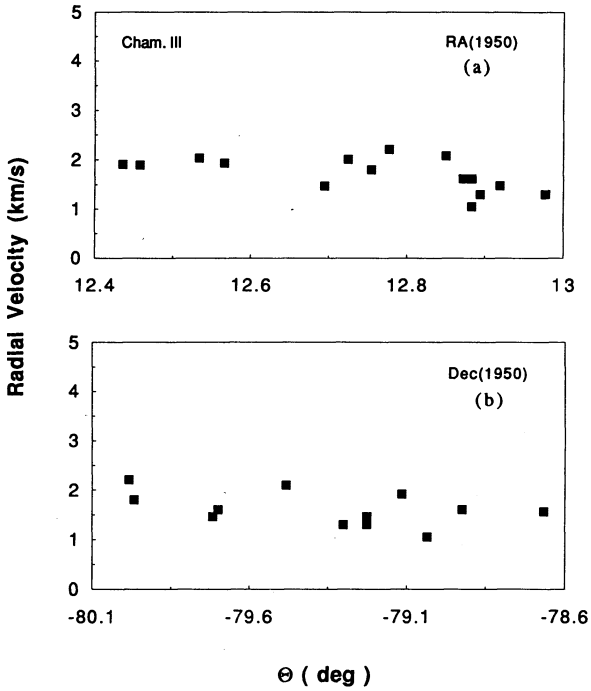

FIG. 10.—Radial velocity-position diagram for the condensations observed in Chamaeleon III cloud. In (*a*) and (*b*) the positions are right ascension and declination, respectively.

8.6. *Star Formation in Musca, Chamaeleon, Taurus, and Ophiuchus*

From 16 positions observed in Musca cloud only one has an *IRAS* source associated that is a good candidate to be a T Tauri star. This *IRAS* source was also indicated by Hetem et al. (1988) as the unique possible T Tauri star in the whole Musca cloud. Thus, considering the number of dense condensations observed in this cloud we find 0.06 as the fraction of condensations associated with young stellar object. As the total mass of the cloud estimated from the extinction distribution is 200 $M_\odot$, and the mass of the T Tauri star is probably less than 1 $M_\odot$, it seems that the star formation efficiency in this cloud is smaller than 0.5%.

From a total of 43 positions observed in the Chamaeleon clouds, 27 of those in Chamaeleon II, only two had *IRAS* sources associated satisfying the selection criteria and are located in Chamaeleon II cloud. No *IRAS* source or pre–main sequence star have been identified associated to the Chamaeleon III positions observed in this survey. Even in the whole cloud no visible or embedded source is detected (Schwartz 1977; Hetem et al. 1988). In this sense, Chamaeleon III is completely different from Chamaeleon I and Chamaeleon II. Its possible that Coalsack is similar to this cloud, but it is very

difficult to state whether the *IRAS* sources observed in Coalsack are or not associated with the clouds behind (Nyman 1991). Cham III seems to be a unique cloud in this survey for which the star formation efficiency is probably zero, within the limit of available observations.

It is remarkable that the condensations in Chamaeleon II, Chamaeleon III, and Musca generally have significantly smaller column densities of dust, ^{13}CO, and $C^{18}O$ than do condensations of similar size, in dark clouds of similar extent, in Taurus and Ophiuchus (§ 6). A similar contrast is also seen by comparison of a recent NH_3 line survey of the southern cores (Fuller, Vilas Boas, & Myers 1994) with the northern core survey of Benson & Myers (1989). The most interesting aspect of this difference is that the condensations in Chamaeleon II, Chamaeleon III, and Musca also have far fewer young stellar objects (YSOs) and far lower star formation efficiency than do Taurus and Ophiuchus (§ 7).

This close association between dark cloud condensations and YSOs has been known for some time (Myers & Benson 1983; Beichman et al. 1986), but no quantitative trend from region to region has so far been reported between condensation properties and the incidence of YSOs. The trend reported here is now evident because the number of regions with enough spectral measurements to allow comparison has increased from two (Taurus and Ophiuchus) to five (Taurus, Ophiuchus, Chamaeleon II, Chamaeleon III, and Musca). We do not include the observed condensations in Cepheus, Vela, and Coalsack in this comparison because they appear to be primarily groups of globules rather than condensations in much more extended clouds. However, including them would only strengthen the apparent trend in the five other regions.

If core column densities increase with time until after they form stars, this trend implies that Chamaeleon II, Chamaeleon III, and Musca have not formed stars in substantial numbers because not enough of their cores are "ready," in contrast to those in Taurus and Ophiuchus. A condition of readiness is evidently a mean column density of $\sim 1 \times 10^{15}$ $C^{18}O$ molecules cm^{-2} in the $J = 1$ level, or $\sim 7 \times 10^{21}$ H_2 cm^{-2}, over an extent ~ 0.2 pc, or more. These properties correspond approximately to those traced by the 1.3 cm line of NH_3 in low-mass "dense cores": a uniform cylinder, aligned along the line of the sight, with these values of column density and diameter has mass 4 $M_\odot$, enough to make a typical low-mass star (0.5 $M_\odot$) with 25% efficiency. If its depth is equal to its diameter, its mean density is 1×10^4 cm^{-3}. It will be interesting to make similar comparisons in other nearby dark clouds, including Perseus and Corona Australis.

9. SUMMARY AND CONCLUSIONS

This paper presents ^{13}CO and $C^{18}O$ J:1–0 line observation in 101 condensations in the Vela region and the dark molecular clouds Musca, Coalsack, and Chamaeleon II and III. The data are compared with a similar survey conducted in dense condensations of dark clouds by MLB and are used to obtain information about the dynamic properties of the surveyed clouds. The main results of this research are as follows.

1. The ^{13}CO and $C^{18}O$ antenna temperatures, line widths and $C^{18}O$ optical depths are smaller in this survey than observed by MLB. The peaks of the ^{13}CO and $C^{18}O$ antenna temperature distributions are smaller by 2 and 1.2 K, respectively. The ^{13}CO line width is smaller by 0.4 km s^{-1}, while $C^{18}O$ is the same and the $C^{18}O$ optical depth is smaller by 0.4. Consequently the molecular hydrogen column densities in Vela, Musca, Chamaeleon, and the Coalsack are less than in Taurus, Ophiuchus, and Cepheus by a factor of 2.

2. Ophiuchus is the cloud with the highest average column density (14×10^{21} cm^{-2}) among the sources observed in MLB and this survey. Their condensations are 4 times denser and their ^{13}CO line width are at least 2 times wider than in the other clouds observed in these surveys. The $C^{18}O$ line width, typically 0.7 km s^{-1}, seems not to change significantly from cloud to cloud.

3. Comparison of the distribution of visual extinction estimated from star counts for 19 condensations observed by MLB and for 47 in this survey suggests lower visual extinctions for the condensations observed in this survey. The peak of the extinction distribution is ~ 3.5 mag for the present survey and ~ 4.5 for Taurus sources observed by MLB. This indicates that the differences in $C^{18}O$ column density in result 1 above, are associated more with differences in total gas column density than with differences in ^{13}CO and $C^{18}O$ abundances.

4. Only 8% of the condensations observed in this survey have an associated *IRAS* point source with T Tauri or "protostar" colors, while this fraction is almost 50% in the MLB survey. This low star formation activity in the observed clouds is probably related to the relatively lower column densities of dust, ^{13}CO and $C^{18}O$ in the condensations observed here, compared to those observed by MLB.

5. The high ratio of $C^{18}O$ to ^{13}CO line width observed in condensations in Vela suggests that most of the ^{13}CO line emission, usually extending well beyond the $C^{18}O$ map in dark clouds, is absent in the Vela globules. This reduction may arise because of the strong ultraviolet radiation field in Vela.

6. The distribution of radial velocity observed toward 26 globules in Vela suggests velocity dispersion of 4.7 km s^{-1} which is at least 2 times higher than previously observed in formaldehyde.

7. In Musca filament the velocity gradient changes from 0.1 km s^{-1} pc^{-1} in one extreme to -0.1 km s^{-1} pc^{-1} in the other. This cloud seems to be better represented by a selfgravitating cylinder than by a sheet of gas seen edge-on.

8. In Chamaeleon III the velocity gradient is 0.2 km s^{-1} pc^{-1} while in Chamaeleon II, if there is any gradient, it is weaker than in Musca. The rms velocity dispersion, density and size observed in these clouds suggests that they are close to virial equilibrium.

J. W. S. V.-B. acknowledges the support of the Fundação de Amparo a Pesquisa de São Paulo (Brasil) Postdoctoral Fellowship and the Smithsonian Astrophysical Observatory for support of a Visiting Scientist position. G. A. F. acknowledges the support of a Harvard-Smithsonian Center for Astrophysics Postdoctoral Fellowship and a National Radio Astronomy Observatory Jansky Fellowship. The authors would like to thank Lars Nyman, Wolfgang Wild, and other staff members of the SEST radio telescope who made these observations possible.

REFERENCES

Beichman, C. A., Myers, P. C., Emerson, J. P., Harris, S., Mathieu, R., Benson, P. J., & Jennings, R. E. 1986, ApJ, 307, 337
Beichman, C. A., Neugebauer, G., Habing, H. J., Clegg, P. E., & Chester, T. J., eds. 1984, *IRAS* Catalogs and Atlases, Explanatory Supplement (Washington, DC: US GPO)
Benson, P., & Myers, P. C. 1989, ApJS, 71, 89
Bohlin, R. C., Savage, B. D., & Drake, J. F. 1978, ApJ, 224, 132
Cernicharo, J. 1991, in Physics of Star Formation and Early Stellar Evolution, ed. C. J. Lada & N. D. Kylafis, NATO ASI Ser. (Dordrecht: Kluwer), 287
Cernicharo, J., & Bachiller, R. 1984, A&AS, 58, 327
Cernicharo, J., & Guelin, M. 1987, A&A, 176, 299
Draine, B. T. 1978, ApJS, 36, 595
Falgarone, E., & Puget, J. L. 1986, A&A, 162, 235
Feitzinger, J. V., & Stuwe, J. A. 1984, A&AS, 58, 365
Forveille, T., Guilloteau, S., & Lucas, R. 1989, Software package for reducing continuum and spectroscopic data, Observatoire de Grenoble
Frerking, M. A., Langer, W. D., & Wilson, R. L. 1982, ApJ, 232, L89
Fuller, G. A., Vilas Boas, J. W. S., & Myers, P. C. 1994, in preparation
Gauvin, L. S., & Strom, K. M. 1992, ApJ, 385, 217
Goss, W. M., Manchester, R. N., Brooks, J. W., Sinclair, M. W., Manefield, G. A., & Danziger, I. J. 1980, MNRAS, 191, 533
Harju, J., Sahu, M., Henkel, C., Wilson, T. L., Sahu, K. C., & Pottash, S. R. 1990, A&A, 233, 197
Harris, S. 1985, in Proc. ESO-IRAM-Onsala Workshop on Submillimeter Astronomy, ed. P. A. Shaver & K. Kjar (Sweden: ESO), 527
Harris, S., Clegg, P., & Hughes, J. 1988, MNRAS, 235, 441
Hartley, M., Manchester, R. N., Smith, R. M., Tritton, S. B., & Goss, W. M. 1986, A&AS, 63, 27
Herbig, G. H., & Bell, K. R. 1988, Lick Obs. Bull., No. 1111
Hetem, J. C. G., Sanzovo, G. C., & Lepine, J. R. D. 1988, A&A, 76, 347
Krautter, J. 1991, in Low Mass Star Formation in Southern Molecular Clouds, ed B. Reipurth (Garching: European Southern Observatory), ESO Sci. Rep., No. 110, p. 169
Lada, C. J., & Wilking, B. A. 1984, ApJ, 287, 610
Landman, D. A., Russel-Dupre, R., & Tanigawa, G. 1982, ApJ, 261, 723
Lynds, B. T. 1962, ApJS, 7, 1
McCutcheon, W. H., Roger, R. S., & Dickman, R. L. 1982, ApJ, 256, 139
Murphy, D. C., & Myers, P. C. 1985, ApJ, 298, 818
Myers, P. C. 1985, in Protostars and Planets. II, ed. D. Black & M. Matthews (Tucson: Univ. of Arizona Press), 81
Myers, P. C., & Benson, P. J. 1983, ApJ, 266, 309
Myers, P. C., Linke, R., & Benson, P. J. 1983, ApJ, 264, 517 (MLB)
Myers, P. C., & Fuller, G. A. 1992, ApJ, 396, 631
Myers, P. C., Fuller, G. A., Goodman, A., & Benson, P. J. 1991, ApJ, 376, 561
Myers, P. C., Fuller, G. A., Mathieu, R. D., Beichmann, C. A., Benson, P. J., Schild, R. E., & Emerson, J. P. 1987, ApJ, 319, 340
Nozawa, S., Mizuno, A., Teshima, Y., Ogawa, H., & Fukui, Y. 1991, ApJS, 77, 647
Nyman, L.-Å. 1991, in Low-Mass Star Formation in Southern Molecular Clouds, ESO Sci. Rep. No. 110, ed. B. Reipurth (Garching: ESO), 119
Nyman, L. A., Bronfman, L., & Thaddeus, P. 1991, in Molecular Clouds, ed. R. James & T. Millar (Cambridge Univ. Press), 23
Ostriker, J. 1964, ApJ, 140, 1056
Persi, P., Ferrari-Tonilo, M., Busso, M., Orgilia, L., Roberto, M., Scaltriti, F., & Silvestro, G. 1990, AJ, 99, 303
Reipurth, B. 1983, A&A, 117, 183
Rodgers, A. W. 1960, MNRAS, 120, 163
Schwartz, R. D. 1977, ApJS, 35, 161
Shu, F. H., Adams, F. C., & Lizano, S. 1987, ARA&A, 25, 23
Taylor, K. N., & Storey, J. W. 1984, MNRAS, 209, 5P
Turner, B. E., Rickard, L. J, & Xu, L. 1989, ApJ, 391, 158
Turner, B. E., Xu, L., & Rickard, L. J. 1992, ApJ, 391, 158
van Dishoeck, E. F., & Black, J. H. 1988, ApJ, 334, 771
Weintraub, D. A. 1990, ApJS, 74, 575
Whittet, D. C. B., Prust, T., & Wesselius, P. R. 1991, MNRAS, 249, 319
Zealey, W. J., Ninkov, Z., Rice, E., Hartley, M., & Tritton, S. B. 1983, ApJ, 23, L119